

Determination of the Zak phase of one-dimensional photonic systems via far-field diffraction

C. Liu*, H.R. Wang*, and H.C. Ong^{a)}

Department of Physics, The Chinese University of Hong Kong, Shatin, Hong Kong, People's Republic of China

Bloch waves in 1D periodic systems carry Zak phase, which plays a key role in determining the band topology. In general, for systems that possess inversion symmetry, the Zak phase of an isolated band is quantized as 0 or π and is associated with the spatial field symmetries at the Brillouin zone center and boundary. The phase is π if the field symmetries are different but is 0 when they are the same. Since the radiation losses from leaky systems are strongly associated with the Bloch waves, one may probe the far-field continuum to determine the Zak phases. Here, we formulate the diffractions from photonic systems at the zone center and boundary and find their spectral profiles reveal the Bloch wave symmetries and thereby the corresponding Zak phase. The field symmetries also generalize the occurrence of bound states in the continuum at high symmetry points. For verification, we have studied the Zak phases of TM plasmonic and TE photonic crystals by electrodynamic simulations and measuring the topological properties of plasmonic crystals using Fourier space diffraction spectroscopy and common path interferometry. In addition, a topological protected interface state is demonstrated when two topological trivial and nontrivial systems are joined together. The results prove our method provides a simple way for characterizing the band topology of non-Hermitian systems via far-fields.

* These authors equally contributed to this work

^{a)} hcong@phy.cuhk.edu.hk

I. INTRODUCTION

Topological physics has attracted a widespread of interest not only in condensed matter physics [1-3] but also in other branches such as ultracold atom [4,5], electromagnetism [6-8], mechanics [9], acoustics [10,11], and oceanography [12]. Much attention in this field is focused on realizing the so-called topologically protected states, which support robust wave propagation against perturbation and disorder [1-12]. To produce such states, two systems that are topologically trivial and nontrivial are brought together to facilitate the occurrence of topological phase transition at the interface. As most of the matters are topologically trivial, the identification and the growth of different classes of topological systems are currently under intensive investigation [13,14]. Likewise, developing methods to characterize the topological properties of the systems is equally important.

In analogy to the Su-Schrieffer-Heeger (SSH) model, the band topology of one-dimensional (1D) periodic systems is determined by Zak phase, γ , which is a geometric phase [15,16]. For a particular ℓ^{th} isolated band, γ_ℓ emerges when the Bloch wave travels adiabatically along the band across the first Brillouin zone from $k = -\pi/P$ to π/P , where P is the period of the system. [16]. If systems possess inversion symmetry, γ_ℓ is quantized as either 0 or π [16]. γ defines the topological invariant of two band systems. For systems that support higher order bands, the topology of the band gap of interest is the summation of all γ below that gap, giving rise to a γ summation that is either even or odd multiple of π for indicating whether the system is topologically trivial or nontrivial [17,18]. A zero-dimensional interface state is then formed between two odd and even π systems.

One notable feature that comes with γ is the distinctive spatial wave symmetries at the Brillouin zone center and boundary of the band [16-18]. The field symmetries, typically even and odd with respect to the unit cell center, are the same for $\gamma = 0$ system but different when γ

$= \pi$ [18]. The association between γ and the field symmetry can be understood from the standpoint of Wannier function, which sums the Bloch waves carrying all k along a band [19]. Consider the Bloch waves at the zone center and boundary that have the same field symmetry, the Wannier function has either the $W(-x) = W(x)$ or $W(-x) = -W(x)$ spatial dependence, leading to $\gamma = \frac{2\pi}{P} \int_{-\infty}^{\infty} x |W(x)|^2 dx = 0$ [16]. On the other hand, for the waves that exhibit different spatial symmetries at two high symmetry points, the Wannier function now shows $W(-x+P) = W(x)$ or $W(-x+P) = -W(x)$ dependence, which gives $\gamma = \pi$ [16]. Therefore, instead of tracing the Bloch waves one by one along the band to determine γ , one can simply examine the field symmetries. However, how to measure the Bloch wave symmetry remains challenging.

To date, there have been only a few studies focusing on measuring the geometric phase, either Zak or Berry phase. Demler and Bloch are among the first to combine Bloch oscillation and interferometry in a dimerized cold atom system to mobilize the Bloch wave across the Brillouin zone and subsequently measure γ [20,21]. They prove $\gamma = \pi$ evolves when the intercell interaction is stronger than that of intracell. Cardano et al have demonstrated the use of mean displacement method to determine γ in a chiral Floquet system [22]. Such method is then extended to other more generalized SSH systems where the next nearest neighbor interaction is strong enough to break the chiral symmetry [23]. While most of them trace the Bloch waves, Gorlach et al adopt an alternative approach by probing the spectral positions of the dipolar (bright) and quadrupolar (dark) characteristics of far-field radiations, which scale with the topological invariant of the system as deduced by using temporal coupled mode theory (CMT) [24]. When the bright and dark radiation bands are at longer and shorter wavelengths, the system is trivial, but becomes nontrivial upon switching places. However, their method is limited to the lowest band gap at the zone center. Recently, Chan and his coworkers have

formulated that the sign of the reflection phase for wavelengths within the ℓ^{th} band gap can resolves the 0 and π γ_ℓ [17,18]. The determination of γ_ℓ via measuring the reflection phase of the band gap is then demonstrated in several photonic and acoustic systems [25-28].

Here, we further extend the CMT to formulate the diffractions arising from 1D leaky optical systems and show the mirror symmetric diffraction orders taken at the zone center and boundary directly reveal the near-field symmetries and thereby the corresponding γ . It is found the odd and even near-fields dictate the far-field interferences, shaping the symmetries of the radiation profiles as well as the bound states in the continuum (BICs) [29-35] and Fano resonances [36]. To verify the CMT, we first conduct finite-difference time-domain (FDTD) simulations on 1D Au plasmonic and SiO₂/Au photonic crystals which respectively support TM- and TE-polarized surface waves and the results agree very well with the theory. We then fabricate plasmonic crystals (PmCs) with different geometries and measure their polarization- and angle-resolved diffraction and phase profiles by Fourier space spectroscopy and common path interferometry to study γ . Changing the groove width of PmCs leads to band inversion and thus effectively varies the band topology. Finally, a topological protected interface state is demonstrated by joining two topological trivial and nontrivial PmCs together.

II. TEMPORAL COUPLED MODE THEORY

At high symmetry points in 1D Brillouin zone, two degenerate but counter propagating Bloch modes interact with each other to yield two coupled modes separated by an energy gap [37,38]. Such interaction can be described within the framework of CMT [37-40]. As shown in Fig. 1(a), for an optically thick system that possesses inversion symmetry, the dynamics of two mode amplitudes, a_1 and a_2 , taken under TM or TE polarization can be written as:

$$\frac{d}{dt} \begin{bmatrix} a_1 \\ a_2 \end{bmatrix} = i \begin{bmatrix} \tilde{\omega}_o & \tilde{\omega}_c \\ \tilde{\omega}_c & \tilde{\omega}_o \end{bmatrix} \begin{bmatrix} a_1 \\ a_2 \end{bmatrix} + K^T [s_+], \quad (1)$$

where $\tilde{\omega}_o$ and $\tilde{\omega}_c$ are the complex frequency and coupling constant, which are expressed as $\tilde{\omega}_o = \omega_o + i(\Gamma_a + \Gamma_r)/2$ and $\tilde{\omega}_c = \alpha + i\beta$, where ω_o is the resonant angular frequency, Γ_a and Γ_r are the absorption and radiative decay rates, and α and β are the real and imaginary parts of the coupling constant. For a given polarization, the discrete incoming power amplitude vector is $[s_+] = [s_{-N,+} \cdots s_{0,+} \cdots s_{N,+}]^T$, where the subscript N is an integer ≥ 0 . $s_{0,+}$ is denoted as the surface normal power and $s_{\pm N,+}$ are two mirror symmetric powers defined obliquely with respect to the surface normal. $K^T = \begin{bmatrix} \tilde{\kappa}_{-N,1} & \cdots & \tilde{\kappa}_{0,1} & \cdots & \tilde{\kappa}_{N,1} \\ \tilde{\kappa}_{-N,2} & \cdots & \tilde{\kappa}_{0,2} & \cdots & \tilde{\kappa}_{N,2} \end{bmatrix}$, where $\tilde{\kappa}_{N,1}$ and $\tilde{\kappa}_{N,2}$ are the complex in-coupling constants for inputting energy from the continuum to a_1 and a_2 . N depends on the number of available ports, which is governed by the diffraction equation as $m\lambda = P(\sin\theta - \sin\phi_m)$, where m is the diffraction order, θ is the incident polar angle, and ϕ_m is the diffraction angle [41]. For example, as shown in Fig. 1(b), for the lowest band gap at the zone center, $\theta = 0^\circ$ such that only one $m = 0^{\text{th}}$, i.e. $N = 0$, propagating order exists in free space. For the second band gap at the zone boundary where $\lambda = 2P \sin\theta$, two $m = 0^{\text{th}}$ and 1^{st} orders, i.e. $N = \pm 1$, are present at $\phi_m = \pm\theta$. In general, zone center supports an odd number of $2N + 1$ ports including $\tilde{\kappa}_0$ whereas an even number of $2N$ ports are found at zone boundary where $\tilde{\kappa}_0$ is always zero [41].

To see how the field symmetry is revealed, we solve the eigenvalues and eigenvectors of the homogeneous part of Eq. (1). The complex frequencies of the coupled modes are $\tilde{\omega}_\pm = (\omega_o \pm \alpha) + i((\Gamma_a + \Gamma_r)/2 \pm \beta)$, indicating their spectral positions and decay rates depend on α and β . For the real part, we see the spectral positions of the coupled modes are determined by the magnitude and sign of α and they are separated by an energy gap $= 2\alpha$. On the other hand, for the imaginary part, one mode has larger decay rate whereas another one has lower,

featuring the bright and dark modes [42]. In particular, if $\Gamma_r - 2|\beta| = 0$, one coupled mode exhibits zero radiation damping, resulting in a quasi-BIC [34]. The unit eigenvectors are $\begin{bmatrix} a_+ \\ a_- \end{bmatrix} = \sqrt{\frac{1}{2}} \begin{bmatrix} a_1 + a_2 \\ a_1 - a_2 \end{bmatrix}$, which are orthogonal and carry odd and even symmetries with respect to the unit cell center. As a result, for an isolated energy band, $\gamma = 0$ if both the eigenvectors at the zone center and boundary are either a_+ or a_- but π if they are different.

We study the spatial field symmetries of a_{\pm} for TM and TE polarized waves. Leaky evanescent waves are considered here as an example. For TM modes such as Bloch-like surface plasmon polaritons (SPPs) propagating in the x-direction, the magnetic fields of a_+ are $\vec{H}_1 + \vec{H}_2 = Ae^{-k_z z} u_k(x) (e^{ik_x x} - e^{-ik_x x}) \hat{y}$, where A is a constant, k_x and k_z are the propagation constants in the x- and z-directions, and $u_k(x)$ is the periodic function [43]. $u_k(x)$ is assumed to be an even function for simplicity since its symmetry does not affect the Zak phase results.

The corresponding electric fields are

$$\vec{E} = \frac{\nabla \times (\vec{H}_1 + \vec{H}_2)}{-i\omega\epsilon} = \frac{-2A}{\omega\epsilon} e^{-k_z z} u_k(x) (k_z \sin(k_x x) \hat{x} + k_x \cos(k_x x) \hat{z}),$$

revealing the in-plane x- and out-of-plane z-components are odd and even in the x-direction, or $E_x(x) = -E_x(-x)$ and

$E_z(x) = E_z(-x)$. Likewise, for a_- , we have even $E_x(x) = E_x(-x)$ and odd

$E_z(x) = -E_z(-x)$. Conversely, for TE modes such as waveguide modes, the in-plane electric

fields of a_+ and a_- are $2iAe^{-k_z z} u_k(x) \sin(k_x x) \hat{y}$ and $2Ae^{-k_z z} u(x) \cos(k_x x) \hat{y}$, giving rise to

odd $E_y(x) = -E_y(-x)$ and even $E_y(x) = E_y(-x)$, respectively. Therefore, for the in-plane

components, the TM and TE polarized a_+ and a_- are odd (even) and even (odd) in the x (z)-direction.

Once the field symmetries of a_{\pm} are known, their spectral positions will then be deduced via far-field. By using conservation of energy and time reversal symmetry, the outgoing ports are expressed as $[s_-] = C[s_+] + K \begin{bmatrix} a_1 \\ a_2 \end{bmatrix}$, where $[s_-] = [s_{-N,-} \cdots s_{0,-} \cdots s_{N,-}]^T$ and C is the nonresonant scattering matrix [38]. We find the transformation matrix to be $T^T = \sqrt{\frac{1}{2}} \begin{bmatrix} 1 & 1 \\ 1 & -1 \end{bmatrix}$

so that the outgoing fields can now be rewritten as:

$$[s_-] = C[s_+] + T^T K \begin{bmatrix} a_+ \\ a_- \end{bmatrix} = C[s_+] + \sqrt{\frac{1}{2}} \begin{bmatrix} \tilde{\kappa}_{-N,1} + \tilde{\kappa}_{-N,2} \\ \vdots \\ \tilde{\kappa}_{0,1} + \tilde{\kappa}_{0,2} \\ \vdots \\ \tilde{\kappa}_{N,1} + \tilde{\kappa}_{N,2} \end{bmatrix} a_+ + \sqrt{\frac{1}{2}} \begin{bmatrix} \tilde{\kappa}_{-N,1} - \tilde{\kappa}_{-N,2} \\ \vdots \\ \tilde{\kappa}_{0,1} - \tilde{\kappa}_{0,2} \\ \vdots \\ \tilde{\kappa}_{N,1} - \tilde{\kappa}_{N,2} \end{bmatrix} a_- . \quad (2)$$

Eq. (2) can be further simplified by using the relationships between $\tilde{\kappa}_{-n,i}$ and $\tilde{\kappa}_{n,i}$, where $i = 1$ or 2 and $n \leq N$ is the diffraction order. As provided in the Supplementary Information [44], given the fact that both far- and near-fields should follow the same spatial symmetry, the radiation patterns of TM a_{\pm} arising from the interferences between the decay ports should preserve the same in-plane $E_x^F(x) = -E_x^F(-x)$ and $E_x^F(x) = E_x^F(-x)$ dependences, where the superscript F denotes the far-fields, leading to $\tilde{\kappa}_{-n,1} + \tilde{\kappa}_{-n,2} = -(\tilde{\kappa}_{n,1} + \tilde{\kappa}_{n,2})$ and $\tilde{\kappa}_{-n,1} - \tilde{\kappa}_{-n,2} = \tilde{\kappa}_{n,1} - \tilde{\kappa}_{n,2}$ for a_+ and a_- . Likewise, for TE a_{\pm} , $E_y^F(x) = -E_y^F(-x)$ and $E_y^F(x) = E_y^F(-x)$ also give $\tilde{\kappa}_{-n,1} + \tilde{\kappa}_{-n,2} = -(\tilde{\kappa}_{n,1} + \tilde{\kappa}_{n,2})$ and $\tilde{\kappa}_{-n,1} - \tilde{\kappa}_{-n,2} = \tilde{\kappa}_{n,1} - \tilde{\kappa}_{n,2}$. More importantly, both polarizations indicate $\tilde{\kappa}_{n,1} = -\tilde{\kappa}_{-n,2}$ and $\tilde{\kappa}_{-n,1} = -\tilde{\kappa}_{n,2}$, which agree with the fact that the system should fulfill the inversion symmetry requirement. However, $\tilde{\kappa}_{-n,1} (\tilde{\kappa}_{-n,2})$ is not necessarily equal to $\tilde{\kappa}_{n,1} (\tilde{\kappa}_{n,2})$. In addition, for a_+ , $\tilde{\kappa}_{0,1} + \tilde{\kappa}_{0,2} = -(\tilde{\kappa}_{0,1} + \tilde{\kappa}_{0,2})$ implies the normal diffraction order is always missing, resulting in an even number of decay ports at both

the zone center and boundary. Therefore, at the zone center for TM and TE polarizations, Eq. (2) can be reduced as:

$$\begin{bmatrix} s_{-N,-} \\ \vdots \\ s_{0,-} \\ \vdots \\ s_{N,-} \end{bmatrix} = C[s_+] + \sqrt{\frac{1}{2}} \begin{bmatrix} \tilde{\kappa}_{-N} - \tilde{\kappa}_N \\ \vdots \\ 0 \\ \vdots \\ -(\tilde{\kappa}_{-N} - \tilde{\kappa}_N) \end{bmatrix} a_+ + \sqrt{\frac{1}{2}} \begin{bmatrix} \tilde{\kappa}_{-N} + \tilde{\kappa}_N \\ \vdots \\ 2\tilde{\kappa}_0 \\ \vdots \\ \tilde{\kappa}_{-N} + \tilde{\kappa}_N \end{bmatrix} a_-, \quad (3)$$

where the 1,2 subscripts are now dropped. On the other hand, at the zone boundary, the outgoing fields carry the same analytical form as Eq. (3) except $s_{0,-} = 0$ since $\tilde{\kappa}_0 = 0$.

Eq. (3) reveals additional information about the occurrence of quasi-BIC at high symmetry points. In general, quasi-BIC occurs when all the decay ports are zero. Therefore, at the zone center, unless $\tilde{\kappa}_0 = 0$, quasi-BIC can only be observed from a_+ . Particularly, for the lowest zone center band gap where only the $N = 0$ port is present, a a_+ quasi-BIC is always present, making it symmetry protected [34]. However, for higher order band gaps, while the normal $N = 0$ port is still zero, other $N > 0$ ports are not necessary. Quasi-BIC can still be found if $\tilde{\kappa}_{-n} = \tilde{\kappa}_n$. In other words, if all the mirror symmetric decay ports of the uncoupled mode are identical and in-phase, destructive interferences occur everywhere across all diffraction orders, resulting in quasi-BIC. Such special condition can only be met for certain tailored system geometry. If $\tilde{\kappa}_{-n} \neq \tilde{\kappa}_n$, a_+ appears as bright or dark mode depending on the sign of β . On the other hand, at the zone boundary where $s_{0,-}$ is always zero, a_+ or a_- can be quasi-BIC if $|\tilde{\kappa}_n| = |\tilde{\kappa}_{-n}|$ or $|\tilde{\kappa}_n| = -|\tilde{\kappa}_{-n}|$ is fulfilled.

We then explicitly formulate the diffraction orders. By considering only one single incidence port q such that $[s_+] = [\cdots 0 \ s_{q,+} \ 0 \ \cdots]^T$, the coupled mode amplitudes are

$a_+ = \frac{1}{\sqrt{2}} \frac{(\tilde{\kappa}_q - \tilde{\kappa}_{-q})s_{q,+}}{i(\omega - \tilde{\omega}_+)}$ and $a_- = \frac{1}{\sqrt{2}} \frac{(\tilde{\kappa}_q + \tilde{\kappa}_{-q})s_{q,+}}{i(\omega - \tilde{\omega}_-)}$. Two mirror symmetric $n \leq N$ diffraction

orders thus are:

$$\begin{aligned} \frac{s_{-n,-}}{s_{q,+}} &= \tilde{c}_{-n} - \frac{1}{2} \frac{(\tilde{\kappa}_n - \tilde{\kappa}_{-n})(\tilde{\kappa}_q - \tilde{\kappa}_{-q})}{i(\omega - \tilde{\omega}_+)} + \frac{1}{2} \frac{(\tilde{\kappa}_n + \tilde{\kappa}_{-n})(\tilde{\kappa}_q + \tilde{\kappa}_{-q})}{i(\omega - \tilde{\omega}_-)}, \\ \frac{s_{+n,-}}{s_{q,+}} &= \tilde{c}_n + \frac{1}{2} \frac{(\tilde{\kappa}_n - \tilde{\kappa}_{-n})(\tilde{\kappa}_q - \tilde{\kappa}_{-q})}{i(\omega - \tilde{\omega}_+)} + \frac{1}{2} \frac{(\tilde{\kappa}_n + \tilde{\kappa}_{-n})(\tilde{\kappa}_q + \tilde{\kappa}_{-q})}{i(\omega - \tilde{\omega}_-)}, \end{aligned} \quad (4)$$

where $\tilde{c}_{\pm n}$ are the complex nonresonant scattering coefficients. We see from Eq. (4) that the radiations from a_+ and a_- have odd and even symmetries [37]. While a_- gives two in phase diffraction orders, those from a_+ are π out of phase. Therefore, by fitting the magnitude and phase, $|s_{\pm n,-}/s_{q,+}|^2$ and $\arg(s_{\pm n,-}/s_{q,+})$, spectra of any pair of oblique mirror diffraction orders at the zone center and boundary with Eq. (4) to determine their relative phase, the spectral positions $\text{Re}(\tilde{\omega}_{\pm})$ can be deduced to find out whether a_+ or a_- is associated with the energy band of interest.

III. FINITE-DIFFERENCE TIME DOMAIN SIMULATION

We verify the CMT model by FDTD simulations. Two types of optical systems are considered, and they are 1D Au plasmonic and SiO₂/Au photonic crystals. While the plasmonic crystals (PmCs) support TM-polarized Bloch-like SPPs [45], the photonic crystals (PhCs) excite TE waveguide modes [46]. We will present the results of PmCs here and those of the PhCs are provided in the Supplementary Information [44]. For the PmCs, the unit cell is shown in Fig. 2(a), with the period P and groove height H are set at 900 nm and 50 nm, respectively, and the groove width W is varied from 100 and 700 nm with a step size of 150 nm. The corresponding TM-polarized k - and wavelength-resolved total reflectivity, which sums all the diffraction orders, mappings are calculated along the Γ -X direction in Fig 2(b) – (f), showing

the presence of the dispersive ± 1 and -2 Bloch-like SPP bands, which follow the phase matching equation given as $\frac{\epsilon_{Au}}{\epsilon_{Au} + 1} \left(\frac{1}{\lambda} \right)^2 = \left(\frac{k}{2\pi} + \frac{n_{SP}}{P} \right)^2$, where ϵ_{Au} is the dielectric constant of Au and n_{SP} is the SPP band, as illustrated by the dash lines in Fig 2(b) [37,45]. More importantly, one sees ± 1 SPPs cross at $k = 0 \text{ } \mu\text{m}^{-1}$ and $+1$ and -2 SPPs cross at $k = \pi/P \text{ } \mu\text{m}^{-1}$, yielding two band gaps at $\lambda = 925$ and 650 nm for the zone center and boundary. In agreement with the CMT model, the coupled modes exhibit dark and bright radiation characteristics.

We attempt to determine the Zak phase of the $+1$ SPP band. At the zone center for all PmCs, the dark mode is quasi-BIC and located at the $+1$ band for $W = 100 - 400 \text{ nm}$ but flips to the -1 band when W increases further. The corresponding reflectivity spectra are plotted in Fig. 3(a) for illustration, clearly showing only one single reflectivity dip as the bright mode. As a result, we conclude a_+ locates at the $+1$ band for $W = 100 - 400 \text{ nm}$ but flips to the -1 band for wider W . On the other hand, at the zone boundary, we can no longer differentiate the spectral positions of a_{\pm} simply by examining the total reflectivity spectra because two dark and bright modes are present. Since only a pair of mirror symmetric $m = 0^{\text{th}}$ and 1^{st} , or $n = \pm 1$, diffraction orders is available, Fig. 3(b) & (c) show the simulated $|s_{\pm 1, -}/s_{1, +}|^2$ and $\arg(s_{\pm 1, -}/s_{1, +})$ spectra. We fit them by Eq. (4) to determine the corresponding $\text{Re}(\tilde{\omega}_{\pm})$ of two modes and the best fits are displayed as the solid lines. All $\text{Re}(\tilde{\omega}_{\pm})$ of the PmCs are summarized in Table 1, where the high and low energy modes at the zone center and boundary, which correspond to the modes sitting on the $+1$ band, are highlighted. If two highlights are either a_+ or a_- , the Zak phase is 0, but π when they are different. As a result, by comparing the modes at the zone center and boundary of the $+1$ band, we conclude $\gamma = \pi$ for $W = 100, 250, 550 \text{ nm}$ but $\gamma = 0$ for 400 and 700 nm .

To confirm our findings, we have simulated the $|E_z|$ near-field intensity profiles at the zone center and boundary of the +1 band by FDTD in Fig. 4(a) & (b) for different W . At the zone center, we see the $|E_z|$ profiles are even with respect to the groove center for $W = 100 - 400$ nm but change to odd afterwards [18,47]. On the other hand, the profiles at the zone boundary are odd for $W = 100, 250$, and 700 nm but are even for 400 and 550 nm. As a result, the field symmetries indicate $\gamma = \pi$ for $W = 100, 250$ and 550 nm but 0 for 400 and 700 nm, in consistent with the far-field simulations. In addition, we have calculated the near-field patterns across the first Brillouin zone for all PmCs in the Supplementary Information [44] and then employ the Wilson loop method to directly determine γ_ℓ given as $\int_{-\frac{\pi}{P}}^{\frac{\pi}{P}} X_\ell(k) dk$, where $X_\ell(k)$

is the Berry connection given as
$$\frac{i \int_{unit\ cell} u_{\ell k}^*(x) \mathcal{E}(x) \frac{\partial u_{\ell,k}(x)}{\partial k} dx}{\int_{unit\ cell} u_{\ell k}^*(x) \mathcal{E}(x) u_{\ell,k}(x) dx}$$
 [47,48]. The evolutions of the

individual phase difference, which is $X_\ell(k) \Delta k$, of the +1 band as a function of k with $\Delta k = 0.04\pi/P$ are plotted in Fig. 4(c). The integrated areas yield the γ_ℓ phases that once again support our results.

IV. EXPERIMENTAL VERIFICATION

A series of 1D periodic Au rectangular groove PmCs has been fabricated by focused ion beam (FIB) and their scanning electron microscopy (SEM) images are shown in the insets of Fig. 5(a) – (e), showing they have $P = 900$ nm, $H = 50$ nm, and W varying from 100 to 700 nm [47]. After the sample preparation, the PmCs are then transferred to a homebuilt Fourier space optical microscope described in the Supplementary Information for angle- and wavelength-resolved diffraction measurements [44]. Briefly, a supercontinuum generation laser is

illuminated on the sample at a well-defined incident angle θ via the microscope objective lens and the signals from the sample are collected by the same objective lens in which the diffraction orders are projected onto the momentum space [49,50]. By using an aperture to filter out the desired diffraction order, a spectrometer-based CCD detector and a common path interferometer are used for measuring the magnitude and phase spectra [51,52].

By varying θ sequentially and at the same time measuring the total reflection spectra, we contour plot the TM-polarized reflectivity mappings in Fig. 5(a) – (e) for different W along the Γ -X direction. They show ± 1 and -2 SPP bands are present, and the bands are consistent with the phase-matching equation as illustrated by the dash lines. From the mappings, we see at normal incidence, or the zone center, BIC-like mode is always observed near the band gap. The $+1$ band has a_+ for $W = 100 - 400$ nm but a_- for larger W . On the other hand, at the zone boundary where $+1$ and -2 SPPs cross at $\theta \sim 20.5^\circ$, we see the dark and bright modes are found and their positions depend on W . To estimate the spectral positions of a_\pm , we measure the corresponding $m = 0^{\text{th}}$ and 1^{st} , or $n = \pm 1$, reflectivity and TM-TE phase difference spectra in Fig. 6(a) & (b) and fit them by Eq. (4) to determine the $\text{Re}(\tilde{\omega}_\pm)$ in Table 1, which shows the $+1$ band is a_- for $W = 100, 250$ and 700 nm is a_+ for 400 and 550 nm. Therefore, $\gamma = \pi$ for $W = 100, 250$ and 550 nm but $= 0$ for 400 and 700 nm.

Finally, we demonstrate a topologically protected state is formed at the interface between two topological trivial and nontrivial PmCs [47]. We construct a heterostructure by joining two $W = 100$ and 400 nm PmCs together. In prior to joining, we have examined by FDTD the field symmetries at the zone center and boundary of two PmCs and determine the γ_ℓ of the 0 , -1 , and $+1$ SPP bands to be π , π and π for $W = 100$ nm and π , π and 0 for $W = 400$ nm. Therefore, the sums of γ_ℓ give 3π and 2π for $W = 100$ and 400 nm PmCs, indicating the $-2/+1$

energy gaps at the zone boundary are topological nontrivial and trivial. We then simulate the heterostructure supercell as shown in Fig. 7(a) that consists of 14 unit cells of $W = 100$ and 400 nm PmCs on the right- and left-handed sides [47]. Fig. 7(b) shows the TM-polarized k - and wavelength-resolved reflectivity mapping at the zone boundary along the Γ -X direction, clearly demonstrating a localized mode is located at $k = 0.5\pi/P$ or $\theta = 20.5^\circ$, and $\lambda \sim 640$ nm in the mid of the band gap. We also have simulated the wavelength-dependent near-field mapping of the heterostructure. For different wavelengths, the near-field intensities at 20 nm above the surface is simulated across the heterostructure and then contour plotted in Fig. 7(c), showing the interface is located at $x = 0$ μm and the trivial and nontrivial regions are at $x > 0$ μm and < 0 μm , respectively. One sees two strong fields are visible at ~ 620 and 670 nm in the PmC bulk regions away from the interface due to the excitations of the upper and lower coupled modes. However, the strongest field strength is observed at the interface, $x = 0$ μm , at 640 nm, and it decays rapidly into the bulk regions, signifying the presence of a topologically protected interface state [47]. We have prepared the heterostructure by FIB and its SEM image is shown in Fig. 7(d) with $W = 100$ and 400 nm PmCs on the right- and left-hand sides. The TM-polarized k - and wavelength-resolved reflectivity mapping of the sample is illustrated in Fig. 7(e), showing an interface state is found at $\theta = 20.5^\circ$ and $\lambda \sim 625$ nm in the $+1/-2$ band gap at the zone boundary.

V. CONCLUSION

In summary, we have formulated an analytical model based on temporal CMT to determine the Zak phase of an isolated band in leaky photonic systems. At the Brillouin zone center and boundary, as the far- and near-fields of the systems share the same spatial symmetry, the mirror symmetric diffractions are either in or π out of phase depending on the Bloch wave symmetry. Therefore, the near-field symmetries can be probed by studying the diffraction

profiles. In addition, our model generalizes the occurrence of quasi-BIC at the high symmetry points. The interplay between the in-coupling constants of different ports plays a decisive role in manifesting quasi-BICs. For verification, we have studied 1D PmCs and PhCs that support TM- and TE-polarized SPP and waveguide modes by FDTD and the results agree very well with the theory. We also have prepared 1D PmCs by FIB and examined their diffractions by using Fourier space diffraction spectroscopy and common path interferometry for determining the Zak phases. In the end, a topological protected interface state is demonstrated by joining two topological trivial and nontrivial PmCs together.

VI. ACKNOWLEDGMENT

This research was supported by the Chinese University of Hong Kong through Area of Excellence (AoE/P-02/12) and Innovative Technology Fund Guangdong-Hong Kong Technology Cooperation Funding Scheme (GHP/077/20GD).

Reference

1. X.L. Qi and S.C. Zhang, Topological insulators and superconductors, *Rev. Mod. Phys.* 83, 1057 (2011).
2. M.Z. Hasan and C.L. Kane, Topological insulators, *Rev. Mod. Phys.* 82, 3045 (2010).
3. J.E. Moore, The birth of topological insulators, *Nature* 464, 194 (2010).
4. N.R. Cooper, J. Dalibard, and I.B. Spielman, Topological bands for ultracold atoms, *Rev. Mod. Phys.* 91, 015005 (2019).
5. D.W. Zhang, Y.Q. Zhu, Y.X. Zhao, H. Yan, S.L. Zhu, Topological quantum matter with cold atoms, *Adv. Phys.* 67, 253 (2019).
6. T. Ozawa, H.M. Price, A. Amo, N. Goldman, M. Hafezi, L. Lu, M.C. Rechtsman, D. Schuster, J. Simon, O. Zilberberg, and I. Carusotto, Topological photonics, *Rev. Mod. Phys.* 91, 015006 (2019).
7. L. Lu, J.D. Joannopoulos and M. Soljačić, Topological photonics, *Nat. Photon.* 8, 821 (2018).
8. A.B. Khanikaev and G. Shvets, Two-dimensional topological photonics, *Nat. Photon.* 11, 763 (2017).
9. S.D. Huber, Topological mechanics, *Nat. Phys.* 12, 621 (2016).
10. Z. Yang, F. Gao, X. Shi, X. Lin, Z. Gao, Y.D Chong, and B. Zhang, Topological Acoustics, *Phys. Rev. Lett.* 114, 114301 (2015).
11. G. Ma, M. Xiao and C.T. Chan, Topological phases in acoustic and mechanical systems, *Nat. Rev. Phys.* 1, 281 (2019).
12. P. Delplace, J.B. Marston, and A. Venaille, Topological origin of equatorial waves, *Science* 358, 1075 (2017).
13. F. Tang, H.C. Po, A. Vishwanath, and X. Wan, Comprehensive search for topological materials using symmetry indicators, *Nature* 566, 486 (2019).

14. X. Chen, X. Ma, K. He, J.F. Jia, and Q.-K. Xue, Molecular beam epitaxial growth of topological insulators, *Adv. Mater.* 23, 1162 (2011).
15. W. P. Su, J. R. Schrieffer, and A. J. Heeger, Solitons in Polyacetylene, *Phys. Rev. Lett.* 42, 1698 (1979).
16. J. Zak, Berry's Phase for Energy Bands in Solids, *Phys. Rev. Lett.* 62, 2747 (1989).
17. M. Xiao, Z.Q. Zhang, and C.T. Chan, Surface impedance and bulk band geometric phases in one-dimensional systems, *Phys. Rev. X* 4, 021017 (2014).
18. M. Xiao, G. Ma, Z. Yang, P. Sheng, Z.Q. Zhang, and C.T. Chan, Geometric phase and band inversion in periodic acoustic systems, *Nat. Phys.* 11, 240 (2015).
19. J.K. Asbóth, L. Oroszlány, and A. Pályi, *A Short Course on Topological Insulators* (Springer, New York, 2016).
20. D.A. Abanin, T. Kitagawa, I. Bloch, and E. Demler, Interferometric approach to measuring band topology in 2D optical lattices, *Phys. Rev. Lett.* 110, 165304 (2013).
21. M. Atala, M. Aidelsburger, J.T. Barreiro, D. Abanin, T. Kitagawa, E. Demler and I. Bloch, Direct measurement of the Zak phase in topological Bloch bands, *Nat. Phys.* 9, 795 (2013).
22. F. Cardano, A. D'Errico, A. Dauphin, M. Maffei, B. Piccirillo, C. de Lisio, G. De Filippis, V. Cataudella, E. Santamato, L. Marrucci, M. Lewenstein, and P. Massignan, Detection of Zak phases and topological invariants in a chiral quantum walk of twisted photons, *Nat. Comm.* 8, 15516 (2017).
23. Z. Jiao, S. Longhi, X. Wang, J. Gao, W. Zhou, Y. Wang, Y. Fu, L. Wang, R. Ren, L.-F. Qiao, and X.-M. Jin, Experimentally detecting quantized Zak phases without chiral symmetry in photonic lattices, *Phys. Rev. Lett.* 127, 147401 (2021).
24. M.A. Gorlach, X. Ni, D.A. Smirnova, D. Korobkin, D. Zhirihin, A.P. Slobozhanyuk, P.A. Belov, A. Alù, and A.B. Khanikaev, Far-field probing of leaky topological states in all dielectric metasurfaces, *Nat. Comm.* 9, 909 (2018).

25. W. Gao, M. Xiao, C.T. Chan, and W.Y. Tam, Determination of Zak phase by reflection phase in 1D photonic crystals, *Opt. Lett.* 40, 5259 (2015).
26. Q. Wang, M. Xiao, H. Liu, S. Zhu, and C.T. Chan, Measurement of the Zak phase of photonic bands through the interface states of a metasurface/photonic crystal, *Phys. Rev. B* 93, 041415(R) (2016).
27. L. Fan, W. Yu, S. Zhang, H. Zhang, and J. Ding, Zak phases and band properties in acoustic metamaterials with negative modulus or negative density, *Phys. Rev. B* 94, 174307 (2016).
28. W. Zhu, Y. Ding, J. Ren, Y. Sun, Y. Li, H. Jiang, and H. Chen, Zak phase and band inversion in dimerized one-dimensional locally resonant metamaterials, *Phys. Rev. B* 97, 195307 (2018).
29. K. Koshelev, A. Bogdanov, and Y. Kivshar, Engineering with bound states in the continuum, *Opt. Photon. News* 31, 38 (2020).
30. B. Zhen, C.W. Hsu, L. Lu, A.D. Stone, and M. Soljacic, Topological nature of optical bound states in the continuum, *Phys. Rev. Lett.* 113, 257401 (2014).
31. Y. Zhang, A. Chen, W.H. Liu, C.W. Hsu, B. Wang, F. Guan, X. Liu, L. Shi, L. Lu, and J. Zi, Observation of polarization vortices in momentum space, *Phys. Rev. Lett.* 120, 186103 (2018).
32. W. Ye, Y. Gao, and J. Liu, Singular points of polarizations in the momentum space of photonic crystal slabs, *Phys. Rev. Lett.* 124, 153904 (2020).
33. T. Yoda and M. Notomi, Generation and annihilation of topologically protected bound states in the continuum and circularly polarized states by symmetry breaking, *Phys. Rev. Lett.* 125, 053902 (2020).
34. C.W. Hsu, B. Zhen, A.D. Stone, J.D. Joannopoulos, and M. Soljacic, Bound states in the continuum, *Nat. Rev. Mater.* 1, 16048 (2016).

35. H.M. Döeleman, F. Monticone, W. den Hollander, A. Alu, and A.F. Koenderink, Experimental observation of a polarization vortex at an optical bound state in the continuum, *Nat. Photon.* 12 397 (2018).
36. M.F. Limonov, M.V. Rybin, A.N. Poddubny, and Y.S. Kivshar, Fano resonances in photonics, *Nat. Photon.* 11, 543 (2017)
37. Z. L. Cao and H. C. Ong, Determination of the absorption and radiative decay rates of dark and bright plasmonic modes, *Opt. Exp.* 22, 16112 (2014).
38. L. Verslegers, Z. Yu, Z. Ruan, P. B. Catrysse, and S. H. Fan, From electromagnetically induced transparency to superscattering with a single structure: A coupled-mode theory for doubly resonant structures, *Phys. Rev. Lett.* 108, 083902 (2012).
39. H. A. Haus, *Waves and fields in optoelectronics* (Prentice-Hall, New Jersey, 1984).
40. S. Fan, in *Optical Fiber Telecommunications V*, edited by I. P. Kaminow, T. Li, and A. E. Willner (Academic Press, Burlington, 2008).
41. E.G. Loewen and E. Popov, *Diffraction gratings and applications* (CRC Press, New York, 1997).
42. C. Ropers, D. J. Park, G. Stibenz, G. Steinmeyer, J. Kim, D. S. Kim, and C. Lienau, Femtosecond light transmission and subradiant damping in plasmonic crystals, *Phys. Rev. Lett.* 94 113901 (2005).
43. C. Billaudeau, S. Collin, C. Sauvan, N. Bardou, F. Pardo, and J.-L. Pelouard, Angle-resolved transmission measurements through anisotropic two-dimensional plasmonic crystals, *Opt. Lett.* 33, 165 (2008).
44. See Supplementary Materials for the connection between the far- and near-fields from one-dimensional periodic optical system, simulated near-field patterns of the +1 surface plasmon polariton (SPP) band of 1D PmCs across the first Brillouin zone, FDTD simulation results of 1D SiO₂/Au photonic crystals (PhCs), and the Fourier space optical

microscope for angle- and wavelength resolved diffraction mapping and common path interferometry

45. X. Guo, C. Liu, and H. C. Ong, Generalization of the circular dichroism from metallic arrays that support Bloch-like surface plasmon polaritons, *Phys. Rev. Appl.* 15, 024048 (2021).
46. A. Christ, S.G. Tikhodeev, N.A. Gippius, J. Kuhl, and H. Giessen, Waveguide-plasmon polaritons: Strong coupling of photonic and electronic resonances in a metallic photonic crystal slab, *Phys. Rev. Lett.* 91, 183901 (2003).
47. C. Liu and H. C. Ong, Realization of topological superlattices and the associated interface states in one-dimensional plasmonic crystals, *Phys. Rev. B* 106, 045401 (2022).
48. H. Wang, G.-Y. Guo, and J.-H. Jiang, Band topology in classical waves: Wilson-loop approach to topological numbers and fragile topology, *New. J. Phys.* 21, 093029 (2019).
49. B. Huang, F. Yu, and R. N. Zare, Surface plasmon resonance imaging using a high numerical aperture microscope objective, *Anal. Chem.* 79, 2979 (2007).
50. F. Bleckmann, Z. Cherpakova, S. Linden, and A. Alberti, Spectral imaging of topological edge states in plasmonic waveguide arrays, *Phys. Rev. B* 96, 045417 (2017).
51. Z.L. Cao, S.L. Wong, S.Y. Wu, H.P. Ho, and H.C. Ong, High performing phase-based surface plasmon resonance sensing from metallic nanohole arrays, *Appl. Phys. Lett.* 104, 171116 (2014).
52. S.L. Wong and H.C. Ong, Phase difference mapping of two-dimensional metallic nanohole arrays, *Appl. Phys. Lett.* 100, 233102 (2012).

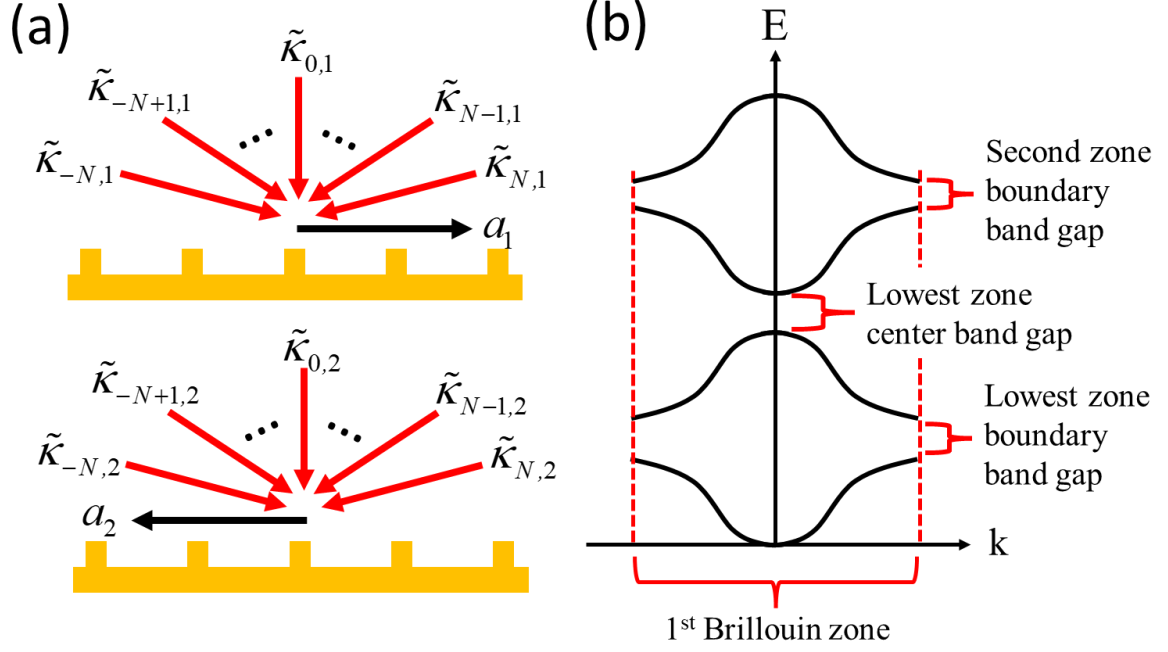


Fig. 1. (a) The schematic shows at the Brillouin zone center and boundary in 1D leaky optical system, two Bloch-like modes $a_{1,2}$ counter propagate in opposite directions with each supports discrete in-coupling channels $\tilde{\kappa}_{N,1,2} \cdots \tilde{\kappa}_{0,1,2} \cdots \tilde{\kappa}_{-N,1,2}$. They interact with each other to form two coupled a_{\pm} at higher and lower energies separated by an energy band gap. (b) $\tilde{\kappa}_{0,1,2} \neq 0$ at the zone center but $\tilde{\kappa}_{0,1,2} = 0$ at the zone boundary.

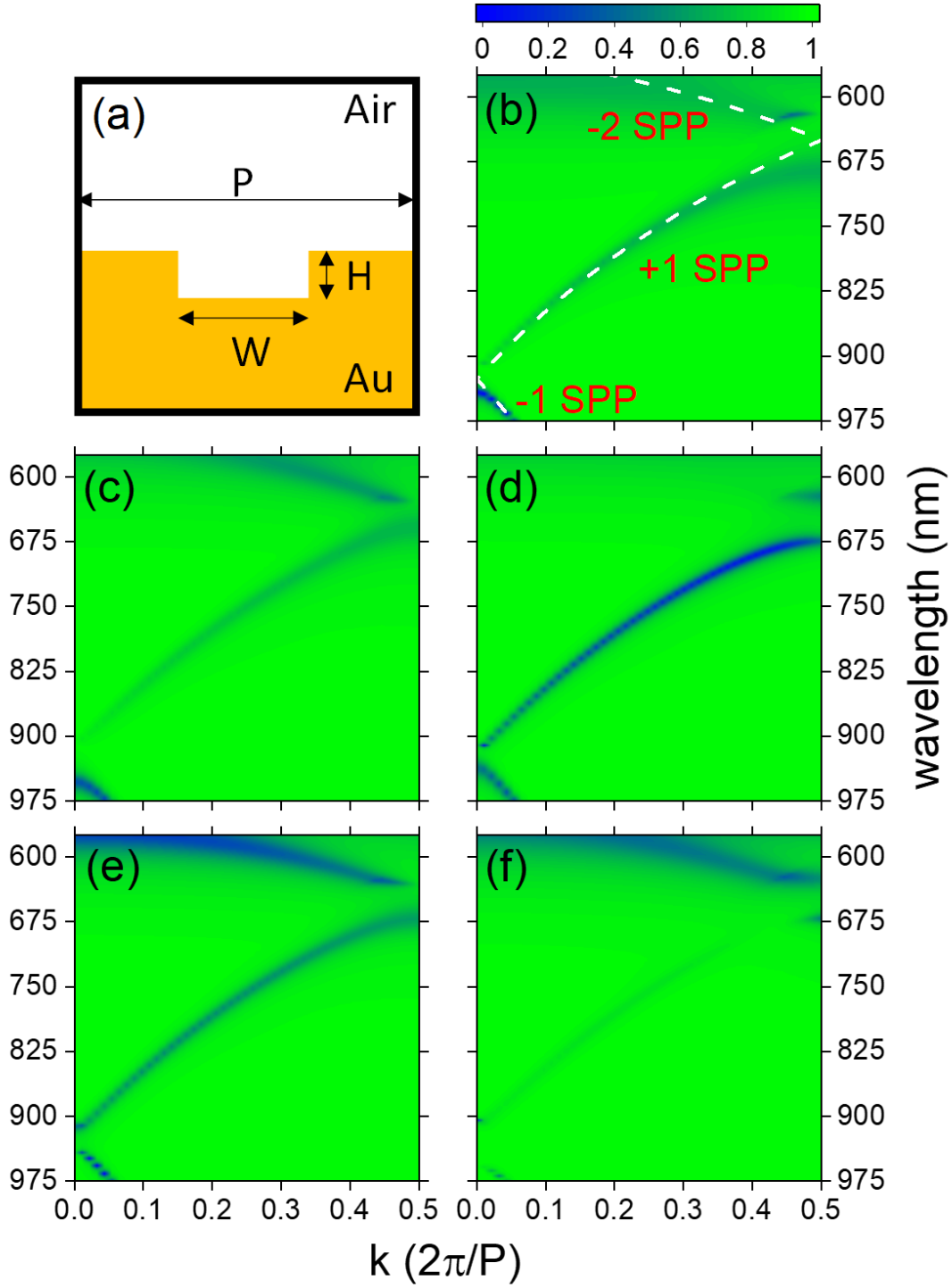


Fig. 2. (a) The unit cell of 1D PmC for FDTD simulations. The simulated TM-polarized k - and wavelength-resolved total reflectivity mappings of PmCs with $W =$ (b) 100, (c) 250, (d) 400, (e) 550, and (f) 700 nm taken along the Γ -X direction. The white dash lines are calculated by using the phase-matching equation, indicating ± 1 and -2 Bloch-like SPPs are excited. At the zone center and boundary where $k = 0$ and 0.5 , two energy band gaps are formed, featuring two dark and bright modes are located above or below the gap. Particularly, at $k = 0$, a quasi-BIC is observed at either above or below the gap.

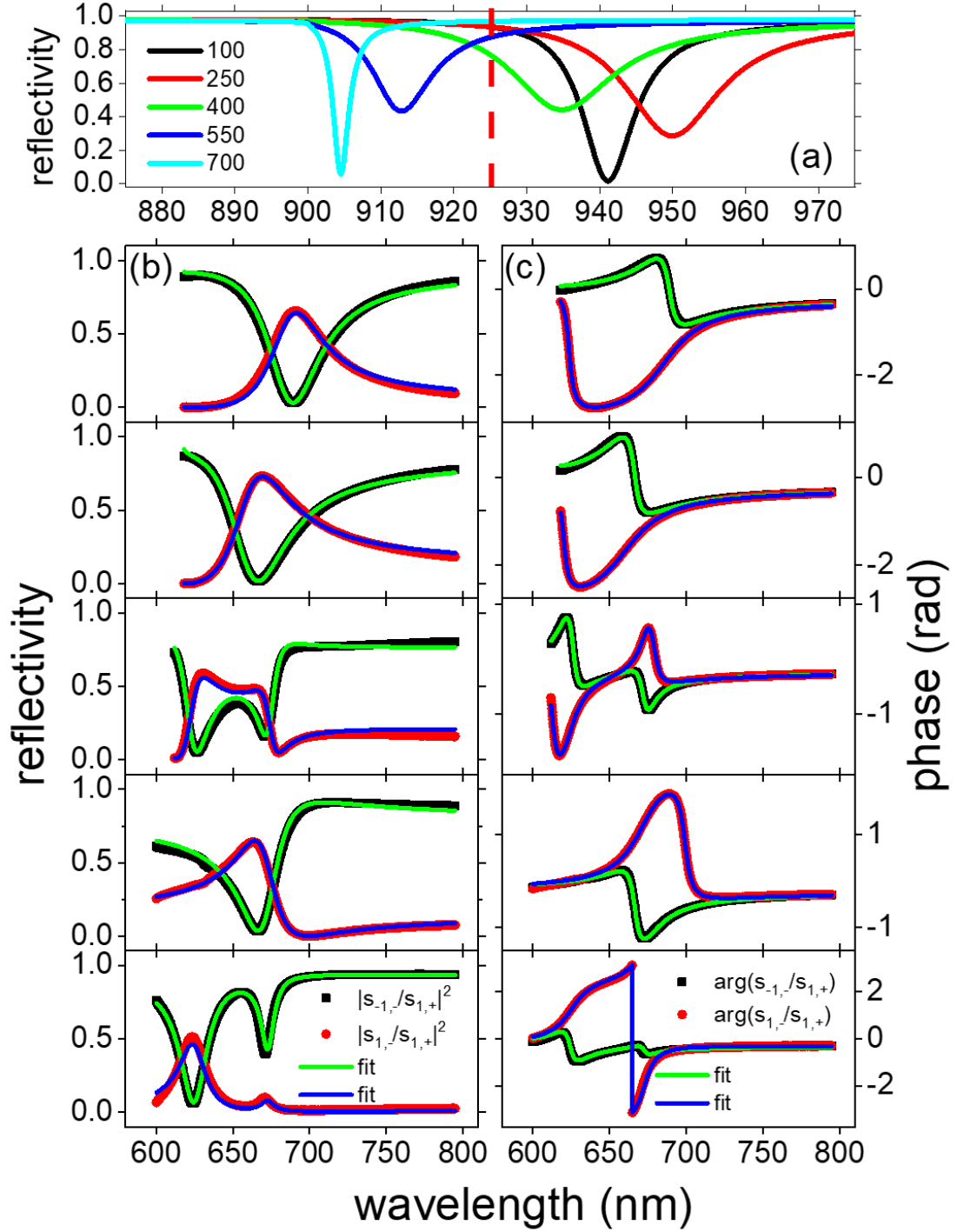


Fig. 3. The TM-polarized total reflectivity spectra of PmCs taken at the zone center for different W , exhibiting only one single reflectivity dip as the bright mode. The red dash line is the band gap center, indicating the quasi-BIC occurs at shorter wavelength for $W = 100, 250$ and 400 nm but longer wavelength for $W = 550$ and 700 nm. At the zone boundary, two TM-polarized mirror symmetric $n = -1$ (black square) and 1 (red circle) (b) reflectivity and (c) phase spectra for $W = 100$ (top) to 700 (bottom). The green and blue solid lines are the best fits determined by CMT.

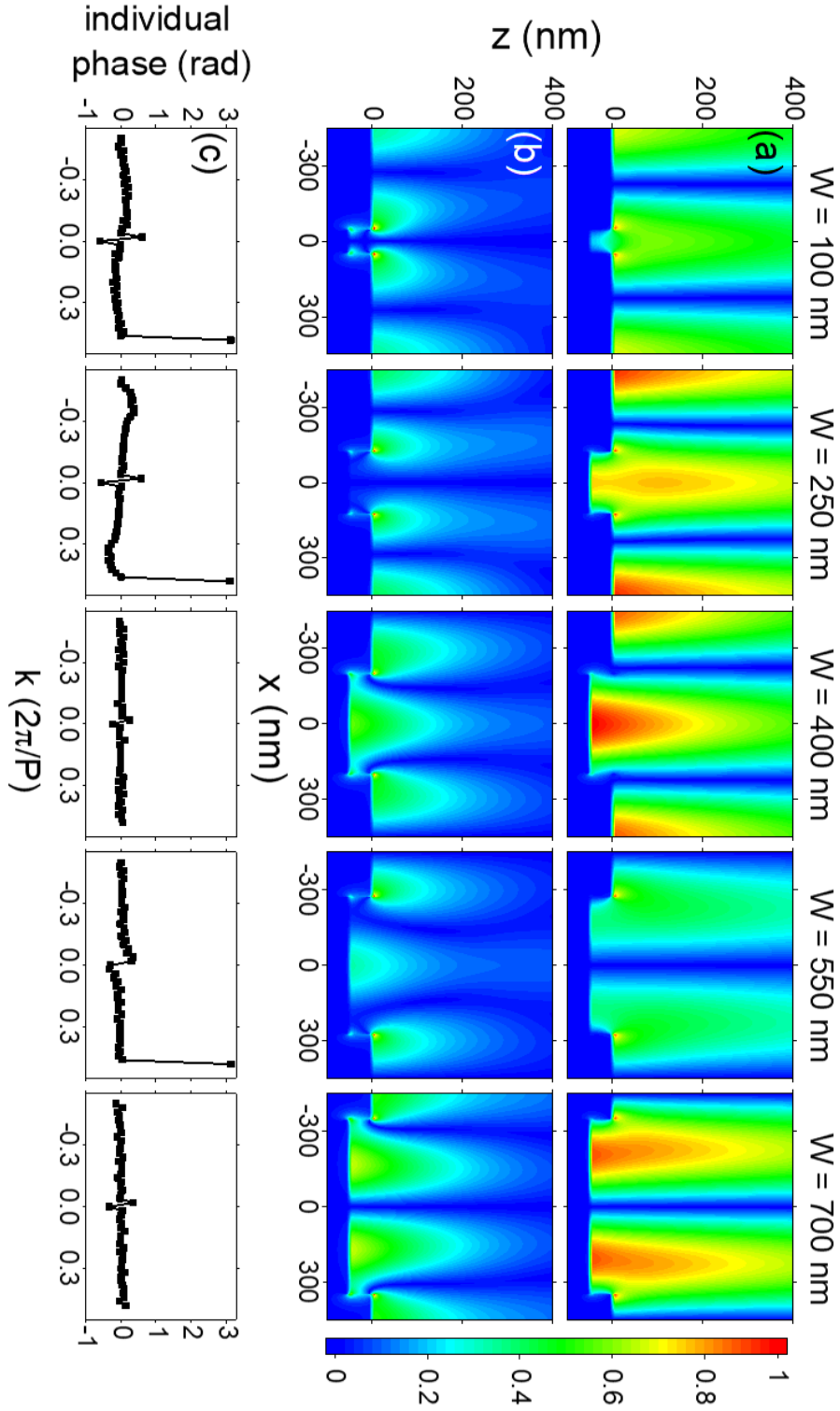


Fig. 4. The FDTD simulated $|E_z|$ near-field patterns of the PmCs for different W taken at the Brillouin zone (a) center and (b) boundary, showing their field symmetries are the same for $W = 400$ and 500 nm but different for $W = 100, 250$, and 700 nm. (c) The individual phase profiles determined by the Wilson loop method. The integration yields the Zak phase, indicating the phase is 0 for $W = 400$ and 500 nm but π for $W = 100, 250$, and 700 nm.

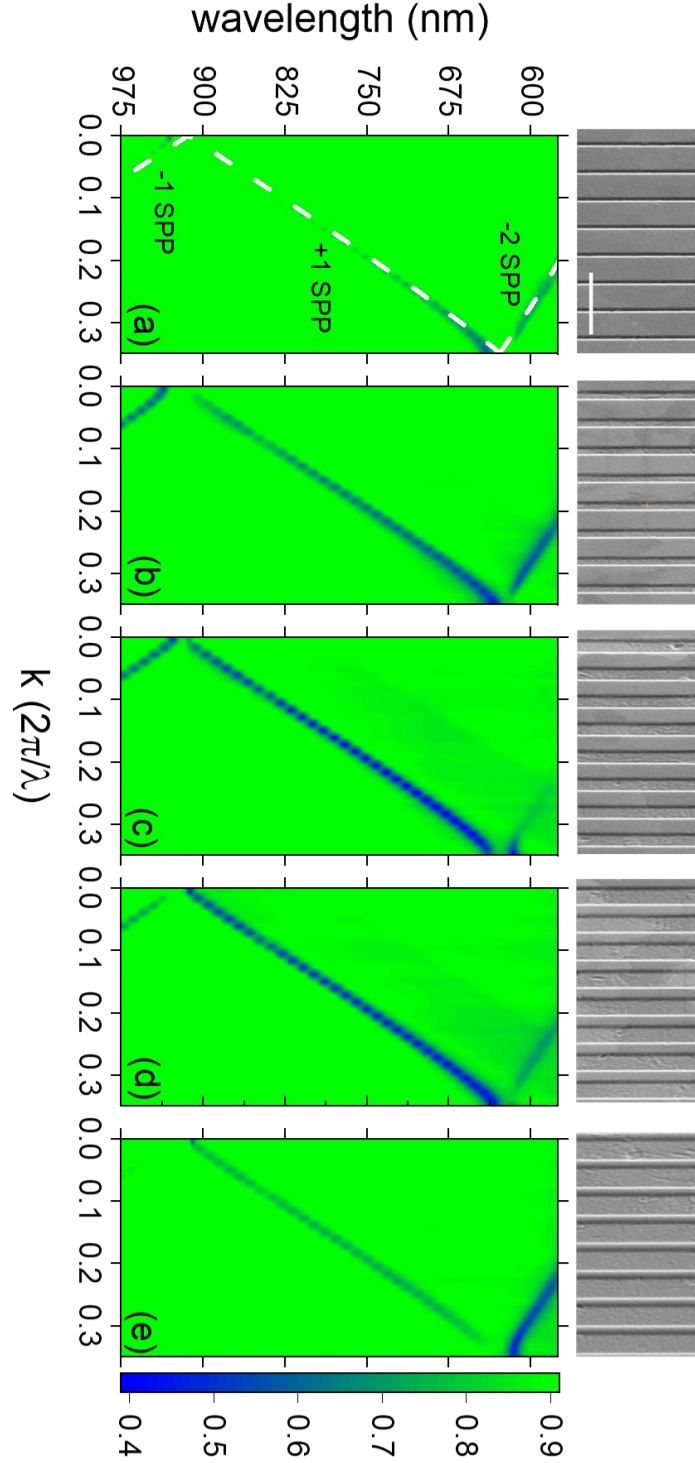


Fig. 5. The measured TM-polarized k - and wavelength-resolved total reflectivity mappings of PmCs with $W =$ (a) 100, (b) 250, (c) 400, (d) 550, and (e) 700 nm taken along the Γ -X direction. The white dash lines are ± 1 and -2 Bloch-like SPPs determined by the phase matching equation. Two band gaps are formed at the zone center and boundary. The insets are the corresponding SEM images of the PmCs with the scale bare = $2\ \mu\text{m}$.

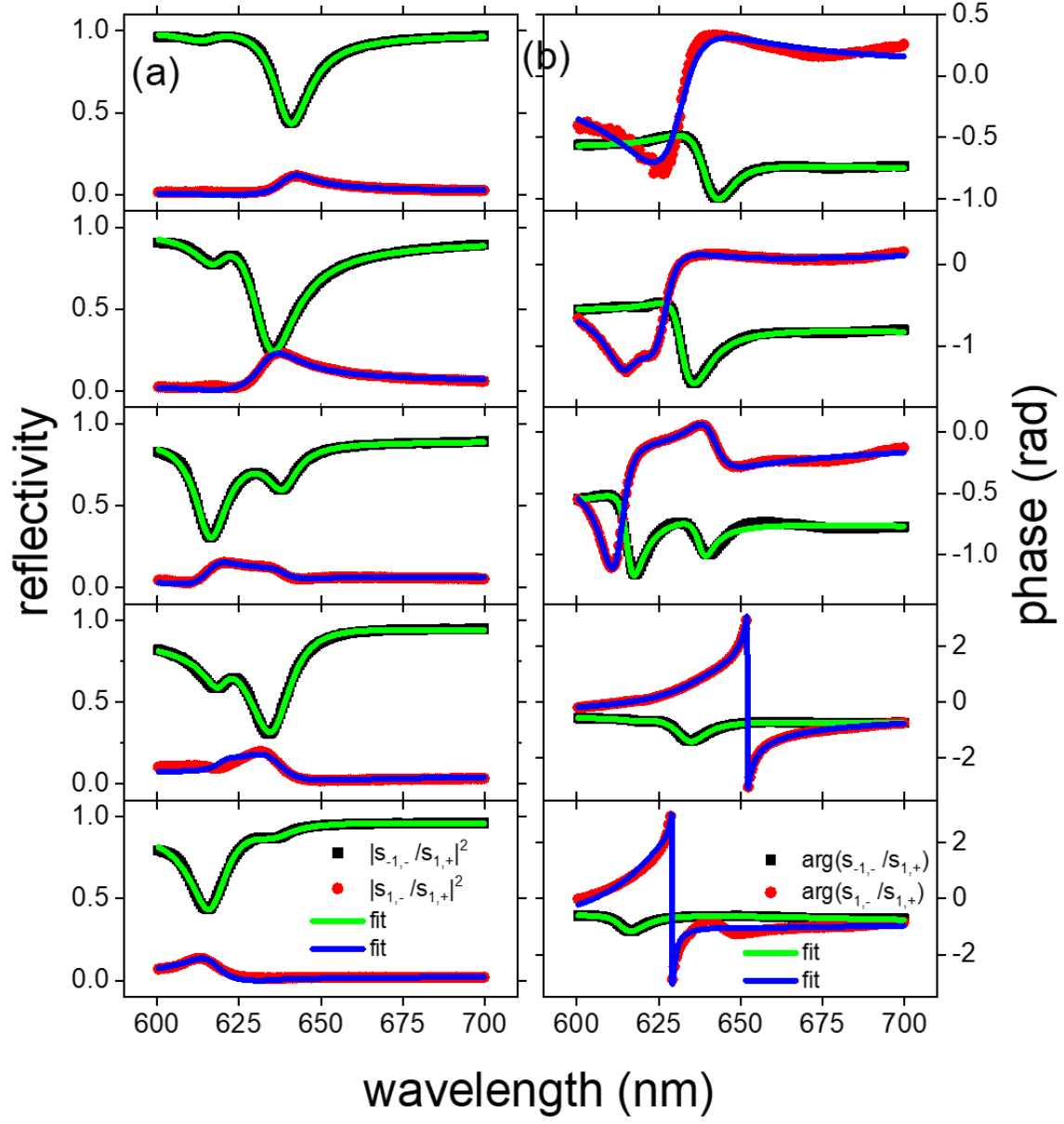


Fig. 6. At the zone boundary, two measured TM-polarized mirror symmetric $n = -1$ (black square) and 1 (red circle) (b) reflectivity and (c) TM-TE phase difference spectra for $W = 100$ (top) to 700 (bottom). The green and blue solid lines are the best fits determined by CMT.

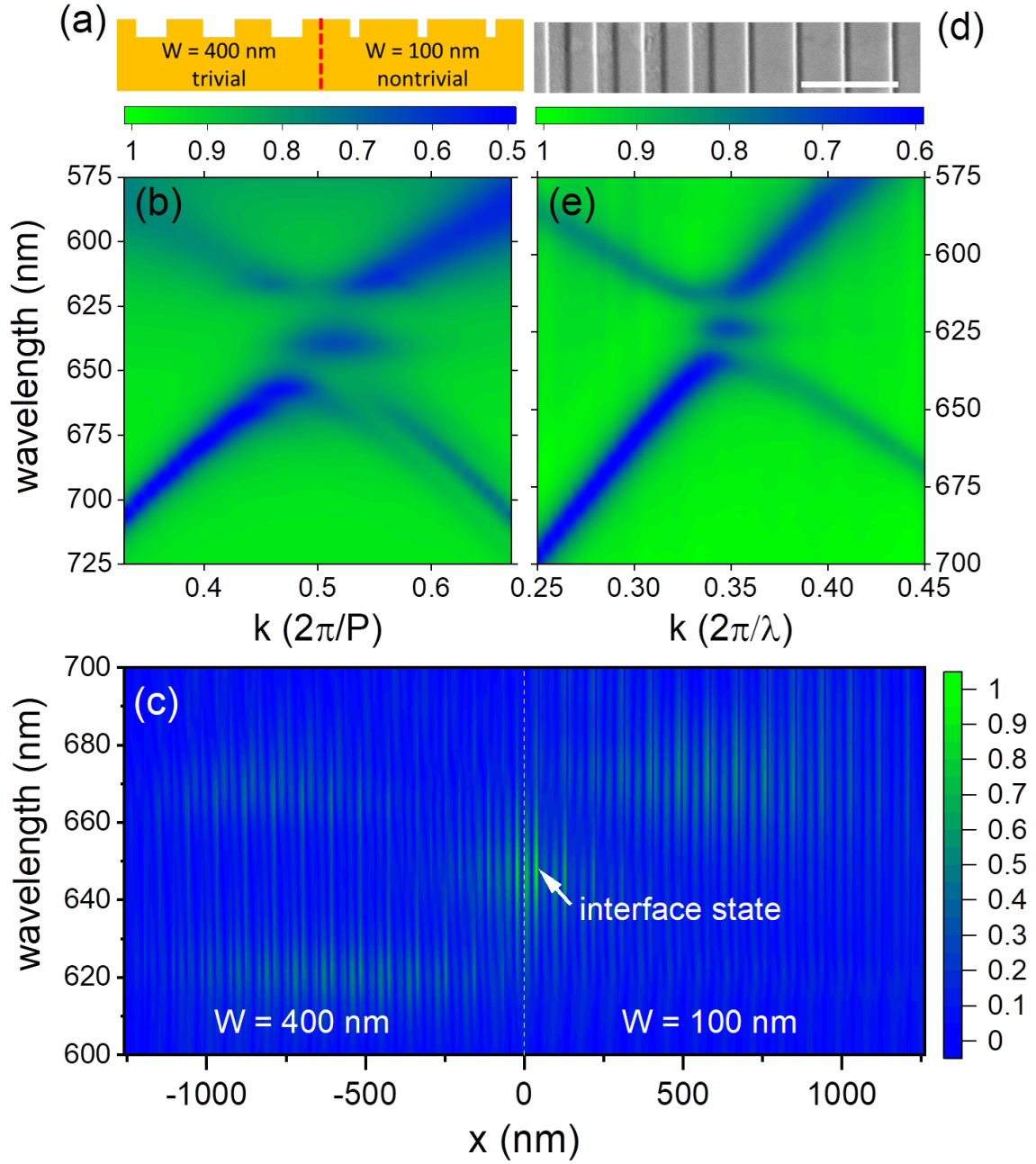


Fig. 7. (a) The schematic of the heterostructure by joining $W =$ nontrivial 100 and trivial 400 nm PmCs. The interface is marked by the dash line. (b) The FDTD simulated TM-polarized reflectivity mapping of the heterostructure taken at the zone boundary along the Γ -X direction, showing an interface state is found within the gap at $\lambda = 640$ nm. (c) The wavelength-dependent near-field intensity mapping simulated at 20 nm above the heterostructure. The interface is located at $x = 0$ μ m, showing strong field localization. The strong fields at 620 and 670 nm arise from the PmC bulk regions. (d) The SEM image of the $W = 100$ and 400 nm with the scale bar corresponding to 2 μ m. (e) The measured TM-polarized reflectivity mapping of the heterostructure taken at the zone boundary along the Γ -X direction, showing an interface state is found within the gap at $\lambda = 625$ nm.

			100 nm	250 nm	400 nm	550 nm	700 nm
FDTD	Zone center	$\text{Re}(\tilde{\omega}_+) \text{ (eV)}$	1.36	1.37	1.36	1.32	1.30
		$\text{Re}(\tilde{\omega}_-) \text{ (eV)}$	1.32	1.31	1.33	1.36	1.37
	Zone boundary	$\text{Re}(\tilde{\omega}_+) \text{ (eV)}$	2.00	1.98	1.84	1.85	1.98
		$\text{Re}(\tilde{\omega}_-) \text{ (eV)}$	1.82	1.89	1.99	1.96	1.85
Experiment	Zone center	$\text{Re}(\tilde{\omega}_+) \text{ (eV)}$	1.36	1.36	1.36	1.33	1.32
		$\text{Re}(\tilde{\omega}_-) \text{ (eV)}$	1.33	1.32	1.34	1.36	1.36
	Zone boundary	$\text{Re}(\tilde{\omega}_+) \text{ (eV)}$	2.02	2.01	1.95	1.96	2.02
		$\text{Re}(\tilde{\omega}_-) \text{ (eV)}$	1.93	1.96	2.02	2.01	1.95

Table 1. The FDTD and experimental $\text{Re}(\tilde{\omega}_{\pm})$ at the Brillouin zone center and boundary for the PmCs with different W. The highlights are the coupled modes located on the +1 SPP band. If the highlights at the zone center and boundary are both a_+ or a_- , the Zak phase is 0. If not, the Zak phase is π .

Supplementary Information

Determination of the band topology of one-dimensional photonic systems via far-field diffraction

C. Liu, H.R. Wang, and H.C. Ong

Department of Physics, The Chinese University of Hong Kong, Shatin, Hong Kong, People's Republic of China

A. Derivation of the connection between the far- and near-fields from one-dimensional periodic optical system

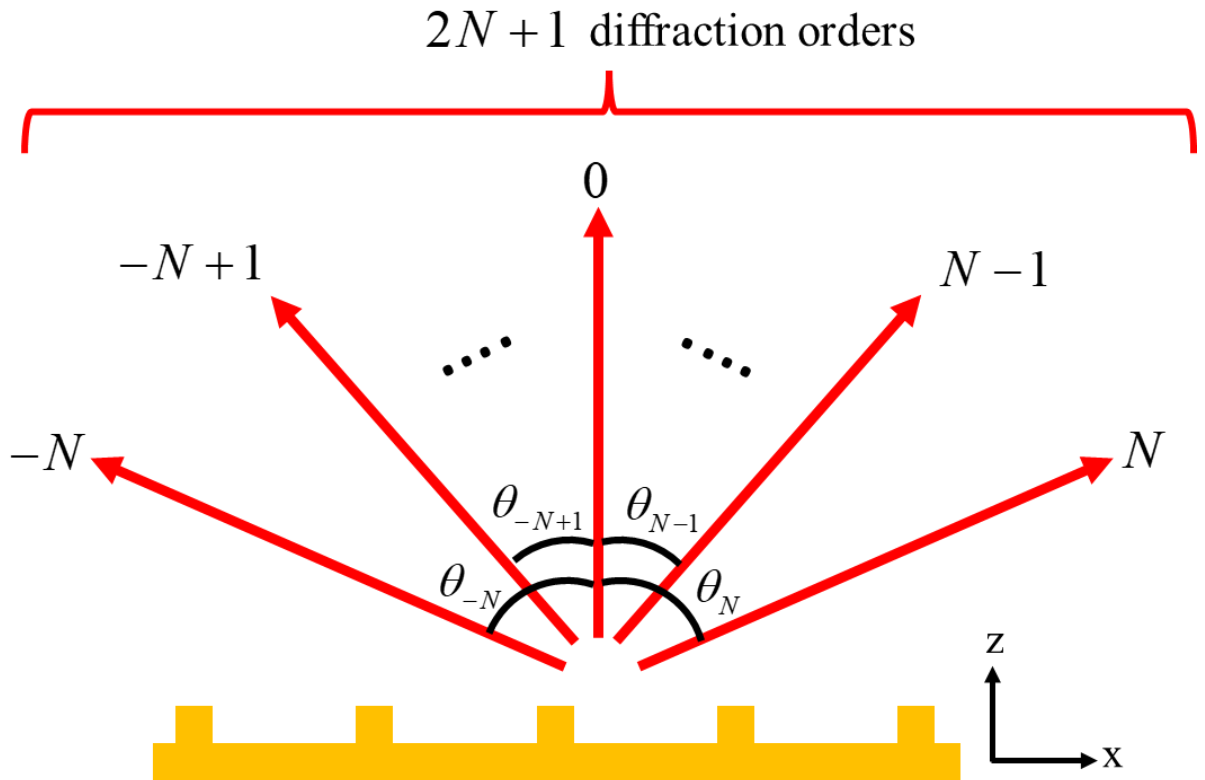


Fig. S1. The schematic of the $2N+1$ diffraction orders arising from the coupled mode supported on 1D periodic leaky system.

As shown in Fig. S1, for a one-dimensional optical leaky periodic system that possesses inversion symmetry in the x-direction, at the Brillouin zone center and boundary, it supports two Bloch-like coupled modes a_{\pm} above and below the photonic band gap with each dissipates a total of $2N + 1$ mirror symmetric diffraction channels in free space, where N is the highest diffraction order. For TM- and TE-polarizations, both the near- and far-fields should carry the same polarization and field symmetry in the x-y plane along the surface. For example, for TM-polarization, in the far-field at z_0 above the system, the x-component of the electric field $E_x^F(x, z_0)$ is expressed as the superposition of all diffraction orders:

$$A_{-N}e^{i\varphi_{-N}}e^{ik\sin\theta_{-N}x}e^{ik\cos\theta_{-N}z_0}\cos\theta_{-N} + A_{-N+1}e^{i\varphi_{-N+1}}e^{ik\sin\theta_{-N+1}x}e^{ik\cos\theta_{-N+1}z_0}\cos\theta_{-N+1} + \dots + A_0e^{i\varphi_0}e^{ikz_0} + \dots + A_{N-1}e^{i\varphi_{N-1}}e^{-ik\sin\theta_{N-1}x}e^{ik\cos\theta_{N-1}z_0}\cos\theta_{N-1} + A_Ne^{i\varphi_N}e^{-ik\sin\theta_Nx}e^{ik\cos\theta_Nz_0}\cos\theta_N, \quad (S1)$$

where A_n , φ_n , and θ_n are the diffraction amplitude, phase, and angle and the subscript n is the diffraction order. At the same time, for the near-field, the TM-polarized a_+ is a standing wave with $\vec{E} \propto e^{-k_z z} u_k(x) (k_z \sin(k_x x) \hat{x} + k_x \cos(k_x x) \hat{z})$, where k_x and k_z are the propagation constants in the x- and z-directions and $u_k(x)$ is the periodic function. Assume $u_k(x)$ is an even function for simplicity, we see $E_x(x)$ is an odd function with $E_x(x) = -E_x(-x)$ dependence. Therefore, Eq. (S1) should also exhibit $E_x^F(x) = -E_x^F(-x)$ dependence, yielding $A_{-n} = A_n$, $\varphi_n = \varphi_{-n} + \pi$, and $A_0 = 0$ that indicate two mirror symmetric diffraction orders have the same magnitude but are always π out of phase and the normal diffraction order is null. As a result, Eq. (S1) is rewritten as:

$$A_Ne^{i\varphi_N}e^{ik\sin\theta_Nx}e^{ik\cos\theta_Nz_0}\cos\theta_N + A_{N-1}e^{i\varphi_{N-1}}e^{ik\sin\theta_{N-1}x}e^{ik\cos\theta_{N-1}z_0}\cos\theta_{N-1} + \dots - A_{N-1}e^{i\varphi_{N-1}}e^{-ik\sin\theta_{N-1}x}e^{ik\cos\theta_{N-1}z_0}\cos\theta_{N-1} - A_Ne^{i\varphi_N}e^{-ik\sin\theta_Nx}e^{ik\cos\theta_Nz_0}\cos\theta_N. \quad (S2)$$

By matching Eq. (S2) with the outgoing power amplitudes of a_+ from CMT, which are

$$\sqrt{\frac{1}{2}} \begin{bmatrix} \tilde{\kappa}_{-N,1} + \tilde{\kappa}_{-N,2} \\ \vdots \\ \tilde{\kappa}_{0,1} + \tilde{\kappa}_{0,2} \\ \vdots \\ \tilde{\kappa}_{N,1} + \tilde{\kappa}_{N,2} \end{bmatrix} a_+, \text{ we conclude } \tilde{\kappa}_{-n,1} + \tilde{\kappa}_{-n,2} = -(\tilde{\kappa}_{n,1} + \tilde{\kappa}_{n,2}) \text{ and } \tilde{\kappa}_{0,1} + \tilde{\kappa}_{0,2} = 0. \text{ Likewise,}$$

for another coupled mode a_- where $\vec{E} \propto e^{-k_z z} u_k(x) (k_z \cos(k_x x) \hat{x} + k_x \sin(k_x x) \hat{z})$, we see

$E_x(x) = E_x(-x)$ and have $A_{-n} = A_n$, $\varphi_n = \varphi_{-n}$ and $A_0 \neq 0$, indicating two mirror symmetric orders are in phase and the normal diffraction order is present. Therefore, Eq. (S1) for a_- is:

$$A_N e^{i\varphi_N} e^{ik \sin \theta_N x} e^{ik \cos \theta_N z_o} \cos \theta_N + A_{N-1} e^{i\varphi_{N-1}} e^{ik \sin \theta_{N-1} x} e^{ik \cos \theta_{N-1} z_o} \cos \theta_{N-1} + \dots + A_0 e^{i\varphi_0} e^{ik z_o} + \dots + A_{N-1} e^{i\varphi_{N-1}} e^{-ik \sin \theta_{N-1} x} e^{ik \cos \theta_{N-1} z_o} \cos \theta_{N-1} + A_N e^{i\varphi_N} e^{-ik \sin \theta_N x} e^{ik \cos \theta_N z_o} \cos \theta_N. \quad (S3)$$

We then have $\tilde{\kappa}_{-n,1} - \tilde{\kappa}_{-n,2} = \tilde{\kappa}_{n,1} - \tilde{\kappa}_{n,2}$ for the outgoing power amplitudes of a_- given as

$$\sqrt{\frac{1}{2}} \begin{bmatrix} \tilde{\kappa}_{-N,1} - \tilde{\kappa}_{-N,2} \\ \vdots \\ \tilde{\kappa}_{0,1} - \tilde{\kappa}_{0,2} \\ \vdots \\ \tilde{\kappa}_{N,1} - \tilde{\kappa}_{N,2} \end{bmatrix} a_- . \quad \text{Finally, two conditions } \tilde{\kappa}_{-n,1} + \tilde{\kappa}_{-n,2} = -(\tilde{\kappa}_{n,1} + \tilde{\kappa}_{n,2}) \quad \text{and}$$

$$\tilde{\kappa}_{-n,1} - \tilde{\kappa}_{-n,2} = \tilde{\kappa}_{n,1} - \tilde{\kappa}_{n,2} \text{ result in } \tilde{\kappa}_{n,1} = -\tilde{\kappa}_{-n,2} \text{ and } \tilde{\kappa}_{-n,1} = -\tilde{\kappa}_{n,2}.$$

On the other hand, for TE-polarized Bloch-like coupled modes a_{\pm} , at z_o in the free space above the system, the y-component of the far-field electric field $E_y^F(x, z_o)$ can be written as:

$$A_{-N} e^{i\varphi_{-N}} e^{ik \sin \theta_{-N} x} e^{ik \cos \theta_{-N} z_o} + A_{-N+1} e^{i\varphi_{-N+1}} e^{ik \sin \theta_{-N+1} x} e^{ik \cos \theta_{-N+1} z_o} + \dots + A_0 e^{i\varphi_0} e^{ik z_o} + \dots + A_{N-1} e^{i\varphi_{N-1}} e^{-ik \sin \theta_{N-1} x} e^{ik \cos \theta_{N-1} z_o} + A_N e^{i\varphi_N} e^{-ik \sin \theta_N x} e^{ik \cos \theta_N z_o}. \quad (S4)$$

The near-field of a_+ where $\bar{E} \propto e^{-k_z z} u_k(x) \sin(k_x x) \hat{y}$, we have $E_y(x) = -E_y(-x)$ such that $A_{-n} = A_n$, $\varphi_n = \varphi_{-n} + \pi$, and $A_0 = 0$, leading to $\tilde{\kappa}_{-n,1} + \tilde{\kappa}_{-n,2} = -(\tilde{\kappa}_{n,1} + \tilde{\kappa}_{n,2})$ and $\tilde{\kappa}_{0,1} + \tilde{\kappa}_{0,2} = 0$. Likewise, for a_- where $E_y(x) = E_y(-x)$, we have $A_{-n} = A_n$, $\varphi_n = \varphi_{-n}$ and $A_0 \neq 0$, giving rise to $\tilde{\kappa}_{-n,1} - \tilde{\kappa}_{-n,2} = \tilde{\kappa}_{n,1} - \tilde{\kappa}_{n,2}$. Therefore, two conditions give the same conclusion that $\tilde{\kappa}_{n,1} = -\tilde{\kappa}_{-n,2}$ and $\tilde{\kappa}_{-n,1} = -\tilde{\kappa}_{n,2}$ regardless of the polarization. As a result, at the zone center for TM- and TE-polarizations, the outgoing profile is:

$$\begin{bmatrix} s_{-N,-} \\ \vdots \\ s_{0,-} \\ \vdots \\ s_{N,-} \end{bmatrix} = C[s_+] + \sqrt{\frac{1}{2}} \begin{bmatrix} \tilde{\kappa}_{-N} - \tilde{\kappa}_N \\ \vdots \\ 0 \\ \vdots \\ -(\tilde{\kappa}_{-N} - \tilde{\kappa}_N) \end{bmatrix} a_+ + \sqrt{\frac{1}{2}} \begin{bmatrix} \tilde{\kappa}_{-N} + \tilde{\kappa}_N \\ \vdots \\ 2\tilde{\kappa}_0 \\ \vdots \\ \tilde{\kappa}_{-N} + \tilde{\kappa}_N \end{bmatrix} a_-, \quad (S5)$$

where the 1,2 subscripts are now dropped. We see quasi-BIC arises from a_+ and it will occur when $\tilde{\kappa}_{-n} - \tilde{\kappa}_n = 0$. However, for the lowest band gap where only the normal diffraction order is present, quasi-BIC always occur, making it symmetry protected. On the other hand, at the zone boundary where $s_{0,-}$ is always 0, we have for TM- and TE-polarizations:

$$\begin{bmatrix} s_{-N,-} \\ \vdots \\ s_{0,-} \\ \vdots \\ s_{N,-} \end{bmatrix} = C[s_+] + \sqrt{\frac{1}{2}} \begin{bmatrix} \tilde{\kappa}_{-N} - \tilde{\kappa}_N \\ \vdots \\ 0 \\ \vdots \\ -(\tilde{\kappa}_{-N} - \tilde{\kappa}_N) \end{bmatrix} a_+ + \sqrt{\frac{1}{2}} \begin{bmatrix} \tilde{\kappa}_{-N} + \tilde{\kappa}_N \\ \vdots \\ 0 \\ \vdots \\ \tilde{\kappa}_{-N} + \tilde{\kappa}_N \end{bmatrix} a_- . \quad (\text{S6})$$

Quasi-BIC occurs depending on the interplay between $\tilde{\kappa}_{-n}$ and $\tilde{\kappa}_n$. a_+ (a_-) is quasi-BIC if $\tilde{\kappa}_{-n} - \tilde{\kappa}_n = 0$ ($\tilde{\kappa}_{-n} + \tilde{\kappa}_n = 0$) but dark and bright modes are present if $\tilde{\kappa}_{-n} \pm \tilde{\kappa}_n \neq 0$.

B. Simulated near-field patterns of the +1 surface plasmon polariton (SPP) band of 1D PmCs across the first Brillouin zone

By using the dipole source excitation method, the complex near-field patterns along the +1 SPP band of 1D Au PmCs with period = 900 nm, groove height = 50 nm and different groove widths have been simulated. The real and imaginary parts of the surface normal components, $\text{Re}(E_z)$ and $\text{Im}(E_z)$, taken at 20 nm above the surface across the Brillouin zone from $k = -\pi/P$ to π/P μm^{-1} are shown in Fig. S2 for groove width $W = 100, 250, 400, 550$ and 700 nm PmCs. They will then be used for determining the Zak phase by the Wilson loop method.

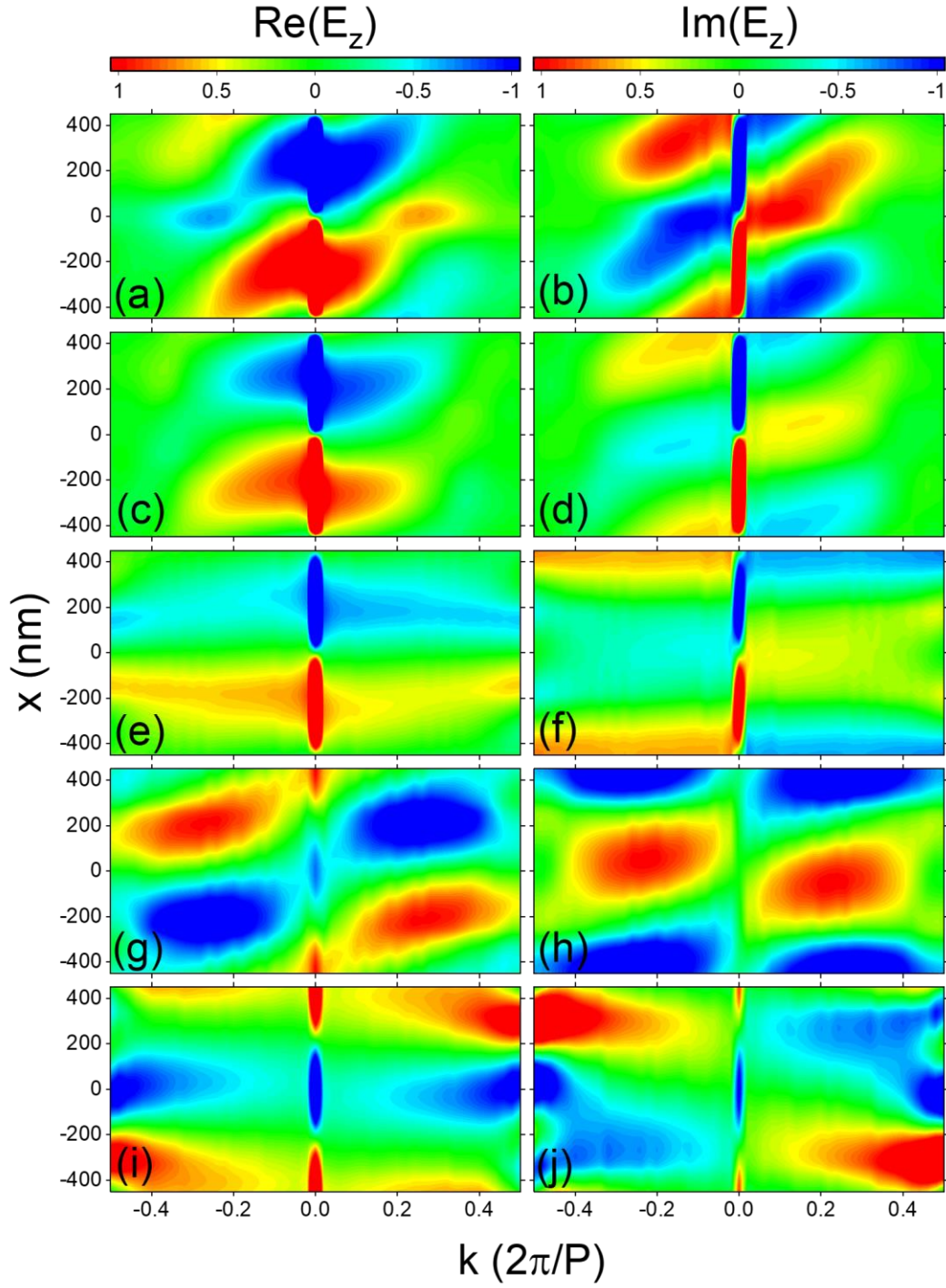


Fig. S2. The real and imaginary parts of the z-component of the $|E_z|$ near-field patterns of the PmCs plotted as a function of k along the +1 SPP band in the first Brillouin zone for different W = (a) & (b) 100, (c) & (d) 250, (e) & (f) 400, (g) & (h) 550, and (i) & (j) 700 nm.

C. FDTD results of 1D SiO₂/Au photonic crystals (PhCs)

Fig. S3(a) shows the unit cell of the PhCs, which has 400 nm thick SiO₂ coated on Au surface with the period P and the groove height H being set at 900 nm and 200 nm whereas the groove width W varied from 100 and 725 nm with a step size of 125 nm. The corresponding TE-polarized k -resolved total reflectivity mappings are shown in Fig S3(b) – (f), showing the dispersive ± 1 and -2 photonic bands, which follow the phase matching equation given as $(n_D/\lambda)^2 = (n_D \sin \theta / \lambda + m_{\text{PhC}}/P)^2$, where n_D is the refractive index of SiO₂ and m_{PhC} is the photonic band. The calculations are superimposed in Fig 3(b). We see $m_{\text{PhC}} = \pm 1$ photonic bands cross at $k = 0 \mu\text{m}^{-1}$ and $m_{\text{PhC}} = +1$ and -2 bands cross at $k = \pi/P \mu\text{m}^{-1}$, yielding two energy band gaps at $\lambda = 930 - 1030$ nm and $700 - 770$ nm at the zone center and boundary. At the zone center, one symmetry protected quasi-BIC is always found, and it is located on the -1 band for $W = 100 - 475$ nm but flips to the $+1$ band when W increases further. At the same time, accidental quasi-BICs are also found along the $+1$ band at different k for all PhCs.

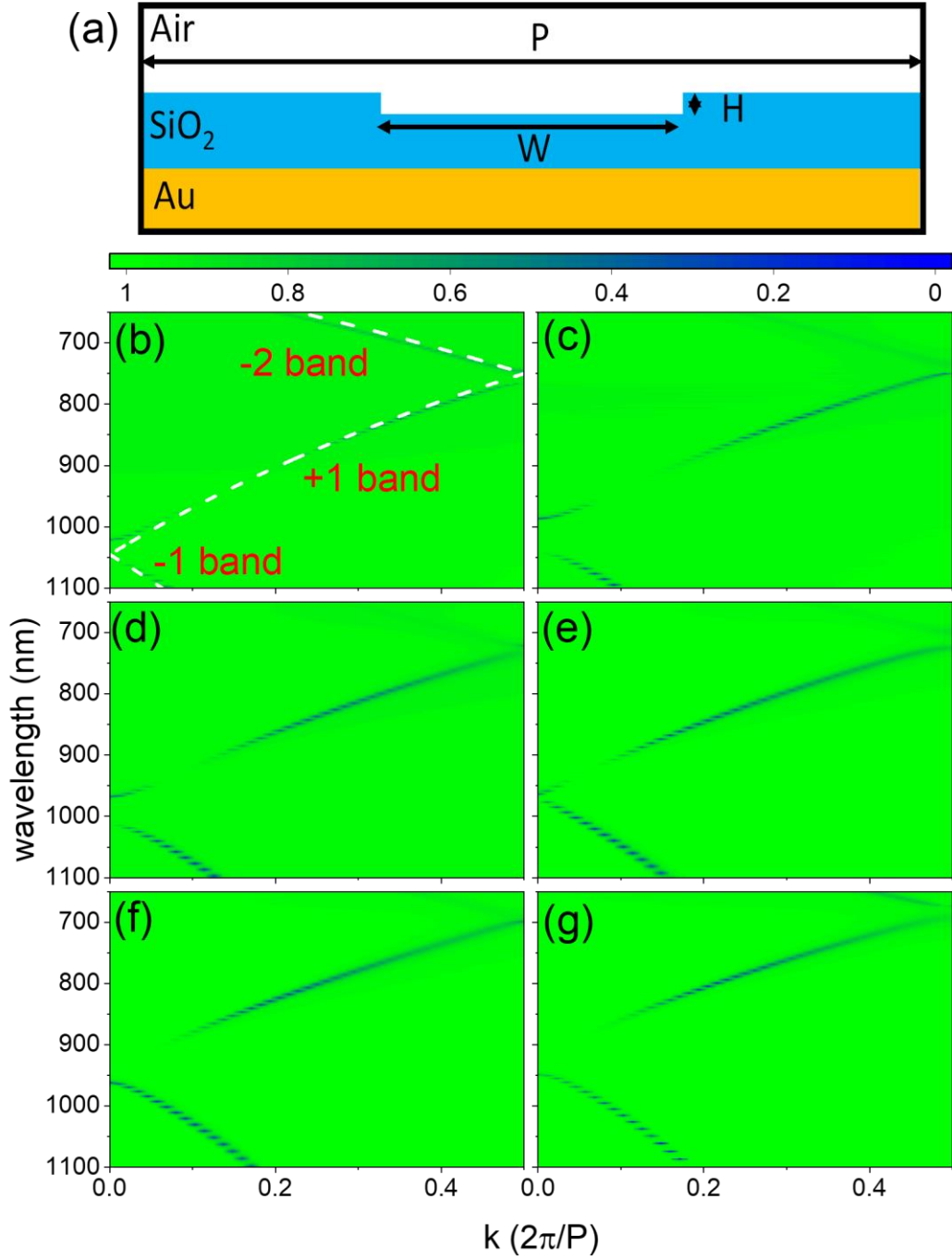


Fig. S3. (a) The FDTD unit cell of the PhC. The simulated TE-polarized k - and wavelength-resolved total reflectivity mappings of PhCs with W = (b) 100, (c) 225, (d) 350, (e) 475, (f) 600, and (g) 725 nm taken along the Γ -X direction. The white dash lines are calculated by using the phase-matching equation, indicating ± 1 and -2 photonic band are present. At the zone center and boundary where $k = 0$ and 0.5 , two energy band gaps are formed, featuring two dark and bright modes are located above or below the gap. Particularly, at $k = 0$, a symmetry protected quasi-BIC is observed at either above or below the gap. On the other hand, an accidentally BIC is observed along the +1 band.

We will focus on the modes located on the +1 band at the zone center and boundary and determine their field symmetries as well as γ . The reflectivity spectra of the PhCs taken under normal incidence, i.e., at the zone center, are illustrated in Fig. S4(a), clearly showing only one single reflectivity dip is present as the bright mode, verifying another coupled mode is quasi-BIC that does not produce any dip. As quasi-BIC arises solely from a_+ for the lowest band gap, we deduce the coupled mode on the +1 band is symmetric a_- for $W = 100 - 475$ nm PhCs but becomes asymmetric a_+ for $W = 600$ and 725 nm PhCs. On the other hand, the reflectivity spectra taken at the zone boundary for all PhCs are shown in Fig. S4(b), showing two bright and dark modes are present.

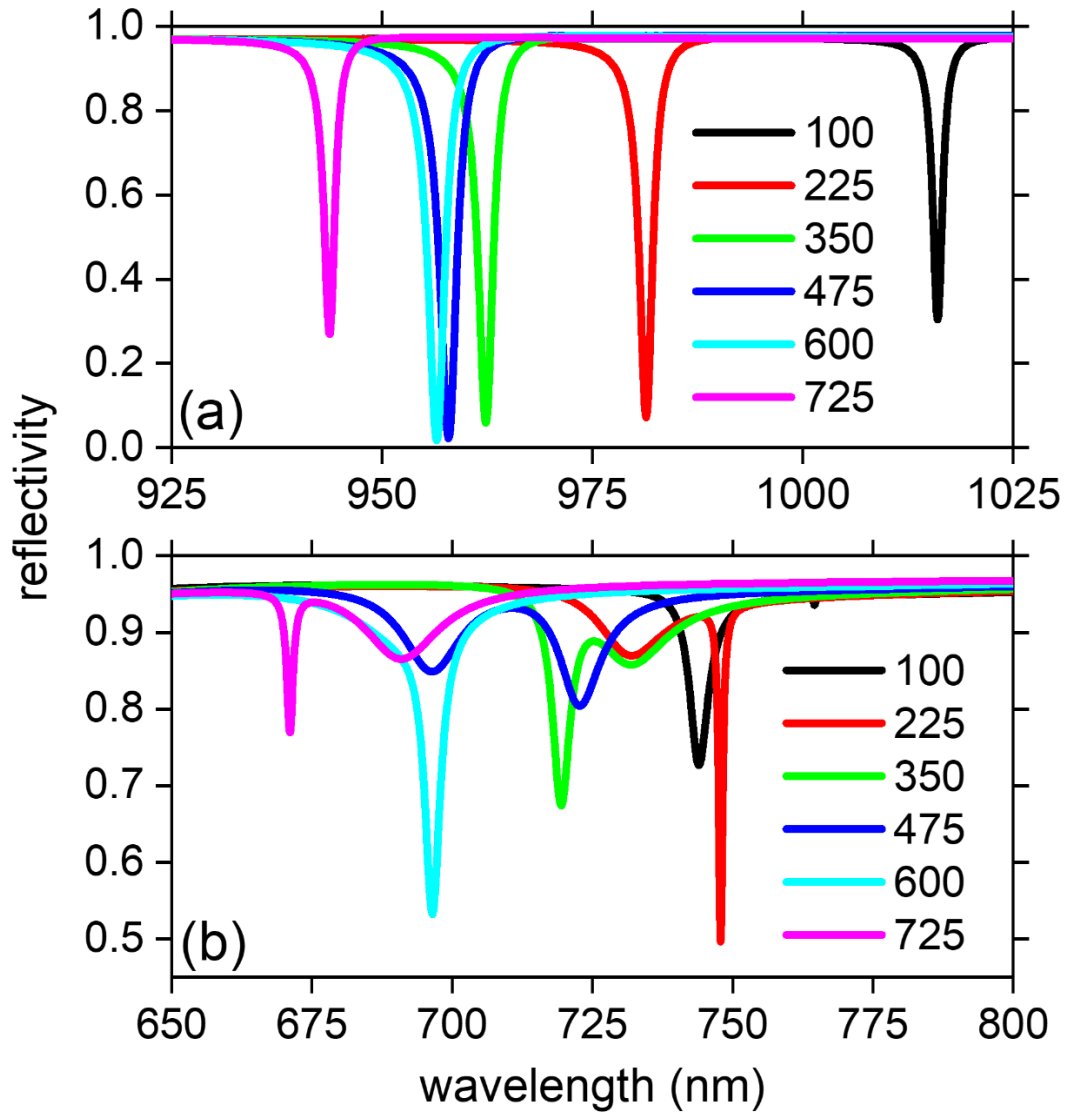


Fig. S4. The TE-polarized total reflectivity spectra of PhCs taken at the zone (a) center and (b) boundary for different W . At the zone center, only one single reflectivity dip is present as the bright mode. On the other hand, at the zone boundary, two bright and dark modes are present.

To determine the near-field symmetries of the PhCs at the zone boundary, the two mirror symmetric diffraction and phase spectra are shown in Fig. S5 and they are fitted with $|s_{\pm 1,-}/s_{1,+}|^2$ and $\arg(s_{\pm 1,-}/s_{1,+})$ from CMT. The best fits are displayed as the solid lines and the fitted $\text{Re}(\tilde{\omega}_{\pm})$ are tabulated in Table S1, in which the highlights are the coupled modes at the zone center (high energy mode) and boundary (low energy mode) sitting on the +1 photonic band. If the highlights at two regions are either a_+ or a_- , the Zak phase is 0, but π when they are different. As a result, we conclude the Zak phase of +1 band for $W = 100, 225$ and 600 nm is π but becomes 0 for $W = 350, 475$ and 725 nm.

		100 nm	225 nm	350 nm	475 nm	600 nm	725 nm
Zone center	$\text{Re}(\tilde{\omega}_+) \text{ (eV)}$	1.18	1.19	1.22	1.27	1.33	1.37
	$\text{Re}(\tilde{\omega}_-) \text{ (eV)}$	1.21	1.26	1.28	1.29	1.29	1.31
Zone boundary	$\text{Re}(\tilde{\omega}_+) \text{ (eV)}$	1.62	1.65	1.72	1.78	1.79	1.79
	$\text{Re}(\tilde{\omega}_-) \text{ (eV)}$	1.67	1.69	1.69	1.71	1.77	1.84

Table S1. The FDTD $\text{Re}(\tilde{\omega}_{\pm})$ at the Brillouin zone center and boundary for the PhCs with different W . The highlights are the coupled modes located on the +1 photonic band. If the highlights at the zone center and boundary are both a_+ or a_- , the Zak phase is 0. If not, the Zak phase is π .

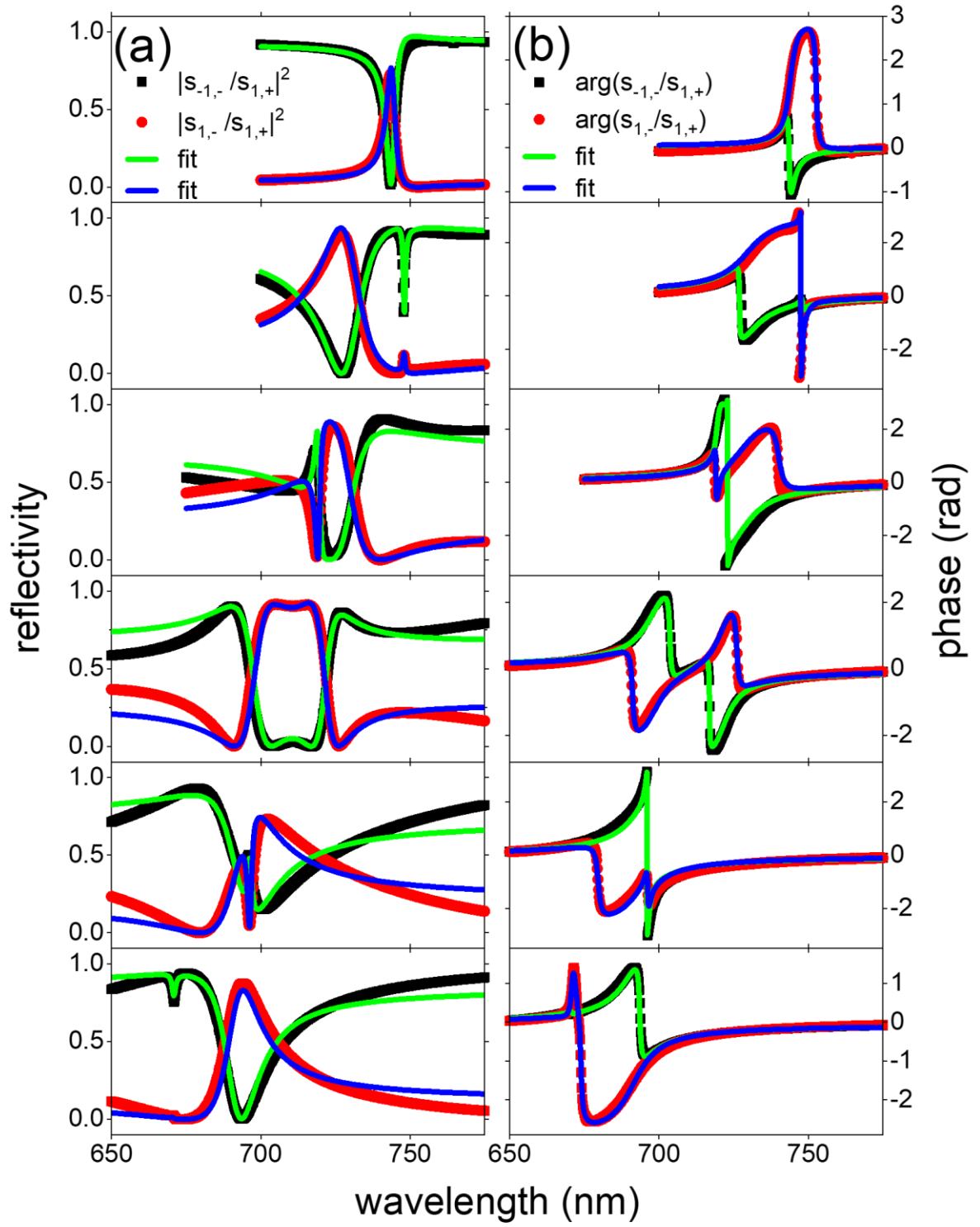


Fig. S5. At the zone boundary, two TE-polarized mirror symmetric $n = -1$ (black square) and 1 (red circle) (a) reflectivity and (b) phase spectra of the PhCs for $W = 100$ (top) to 725 (bottom). The green and blue solid lines are the best fits determined by CMT.

To verify the Zak phases, we have simulated the real and imaginary parts of the surface normal components, $\text{Re}(E_z)$ and $\text{Im}(E_z)$, taken at 20 nm above the surface across the Brillouin zone from $k = -\pi/P$ to $\pi/P \text{ } \mu\text{m}^{-1}$ in Fig. S6 for all PhCs. They will then be used for determining the

Zak phase by the Wilson loop method given as $\int_{-\pi/P}^{\pi/P} X_\ell(k) dk$, where $X_\ell(k)$ is

$$\frac{i \int_{\text{unit cell}} u_{\ell k}^*(x) \mathcal{E}(x) \frac{\partial u_{\ell,k}(x)}{\partial k} dx}{\int_{\text{unit cell}} u_{\ell k}^*(x) \mathcal{E}(x) u_{\ell,k}(x) dx}. \quad \text{The evolutions of the individual phase difference, which is}$$

$X_\ell(k) \Delta k$, of the +1 band as a function of k with $\Delta k = 0.04\pi/P$ of all PhCs are plotted in Fig.

S7. The integrated areas yield the Zak phases are π for $W = 100, 225$, and 600 nm and 0 for $W = 350, 475$ and 725 nm , and they agree very well with earlier CMT results.

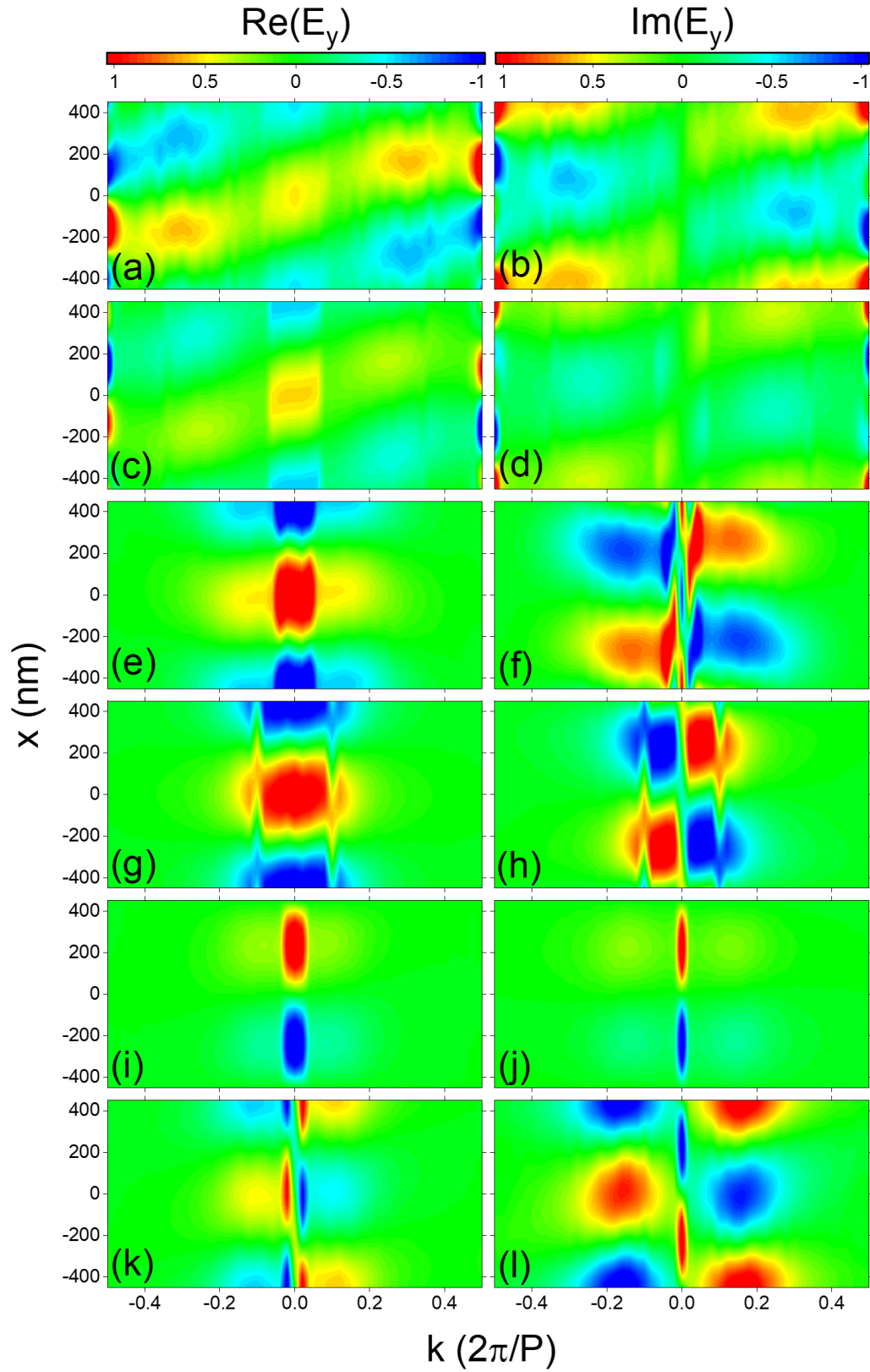


Fig. S6. The real and imaginary parts of the z-component of the near-field patterns of the PhCs plotted as a function of k along the +1 photonic band in the first Brillouin zone for different W = (a) & (b) 100, (c) & (d) 225, (e) & (f) 350, (g) & (h) 475, (i) & (j) 600, and (k) & (l) 725 nm.

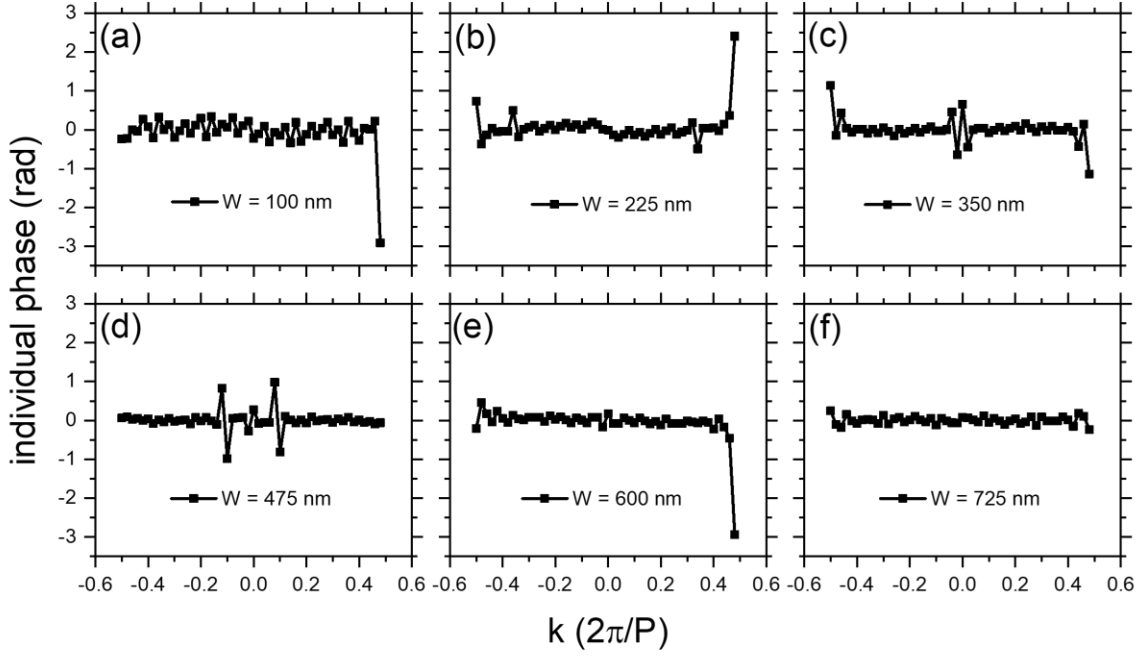


Fig. S7. The individual phase profiles of the PhCs with different W . The integration yields the Zak phase, indicating the phase π for $W = 100, 225$, and 600 nm and 0 for $W = 350, 475$ and 725 nm.

D. Schematic of the Fourier space optical microscope for angle- and wavelength resolved diffraction mapping and common path interferometry

Fig. S8 shows the schematic of the Fourier space optical microscope. Briefly, a broadband supercontinuum laser from a nonlinear photonic crystal fiber is collimated and then passed through a set of linear polarizers, wave plates, and lenses before being focused onto the back focal plane (BFP) of a 100X objective lens (OB) with numerical aperture = 0.9. The light exiting from the objective lens is then a collimated beam with well-defined linear polarization. In addition, by displacing the focused spot across the BFP of the objective lens using a motorized translation stage, the incident polar angle θ of the collimated beam onto the sample can be varied following $\sin\theta = d/f$, where d is the distance between the focused spot and the optical axis of the BFP and f is the focal length of the objective lens. In addition, the azimuth angle ϕ can be varied by a motorized rotation sample stage to align the incident plane to the Γ -X direction of the PmC. The diffractions from the PmC are then collected by the same objective lens and are routed through a set of Fourier lens system so that the diffraction orders are projected onto the momentum space. By placing an aperture at the momentum space to filter

out the desired diffraction order, its intensity and phase spectra can be measured by a spectrometer-based CCD detector and a common path interferometer [1].

To perform common path interferometry, the 45° linearly polarized collimated beam with the Jones vector given as $\frac{1}{\sqrt{2}} \begin{bmatrix} 1 \\ 1 \end{bmatrix}$ is incident on the PmC. The diffraction order from the PmC

after the aperture can be formulated as: $J_{PmC} = \begin{bmatrix} |r_{TM}| e^{i\theta_{TM}} & 0 \\ 0 & |r_{TE}| e^{i\theta_{TE}} \end{bmatrix}$, where $r_{TM,TE}$ and $\theta_{TM,TE}$

are the magnitudes and phases for TM- and TE-polarizations. The diffraction passes through a quarter wave plate with the fast axis being placed at 45° with respect to the incident plane and a motorized rotatable analyzer with angle ξ , which are given as

$J_{analyzer(\xi)} = \begin{bmatrix} \cos^2 \xi & \sin \xi \cos \xi \\ \sin \xi \cos \xi & \sin^2 \xi \end{bmatrix}$ and $J_{QWP(45^\circ)} = \frac{1}{2} \begin{bmatrix} 1-i & 1+i \\ 1+i & 1-i \end{bmatrix}$. The output vector is

$J_{analyzer(\xi)} J_{QWP(45^\circ)} J_{PmC} \frac{1}{\sqrt{2}} \begin{pmatrix} 1 \\ 1 \end{pmatrix}$. After some formulations, the intensities for different $\xi = 0^\circ$,

$\pm 45^\circ$, and 90° can be written as:

$$R_0(\lambda) = \left| \frac{1}{2} \begin{bmatrix} |r_{TM}| e^{i\varphi} + i|r_{TE}| \\ 0 \end{bmatrix} \right|^2 = \frac{1}{4} \left(|r_{TM}|^2 + |r_{TE}|^2 + 2|r_{TM}||r_{TE}|\sin \varphi \right),$$

$$R_{+45}(\lambda) = \frac{1}{4} \left(|r_{TM}|^2 + |r_{TE}|^2 + 2|r_{TM}||r_{TE}|\cos \varphi \right), \quad R_{-45}(\lambda) = \frac{1}{4} \left(|r_{TM}|^2 + |r_{TE}|^2 - 2|r_{TM}||r_{TE}|\cos \varphi \right), \text{ and}$$

$$R_{90} = \frac{1}{4} \left(|r_{TM}|^2 + |r_{TE}|^2 - 2|r_{TM}||r_{TE}|\sin \varphi \right), \text{ where } \varphi = \theta_{TM} - \theta_{TE}. \text{ Therefore, the phase difference}$$

between TM- and TE- polarized diffractions can be calculated by: $\tan \varphi(\lambda) = \frac{R_0(\lambda) - R_{90}(\lambda)}{R_{+45}(\lambda) - R_{-45}(\lambda)}$.

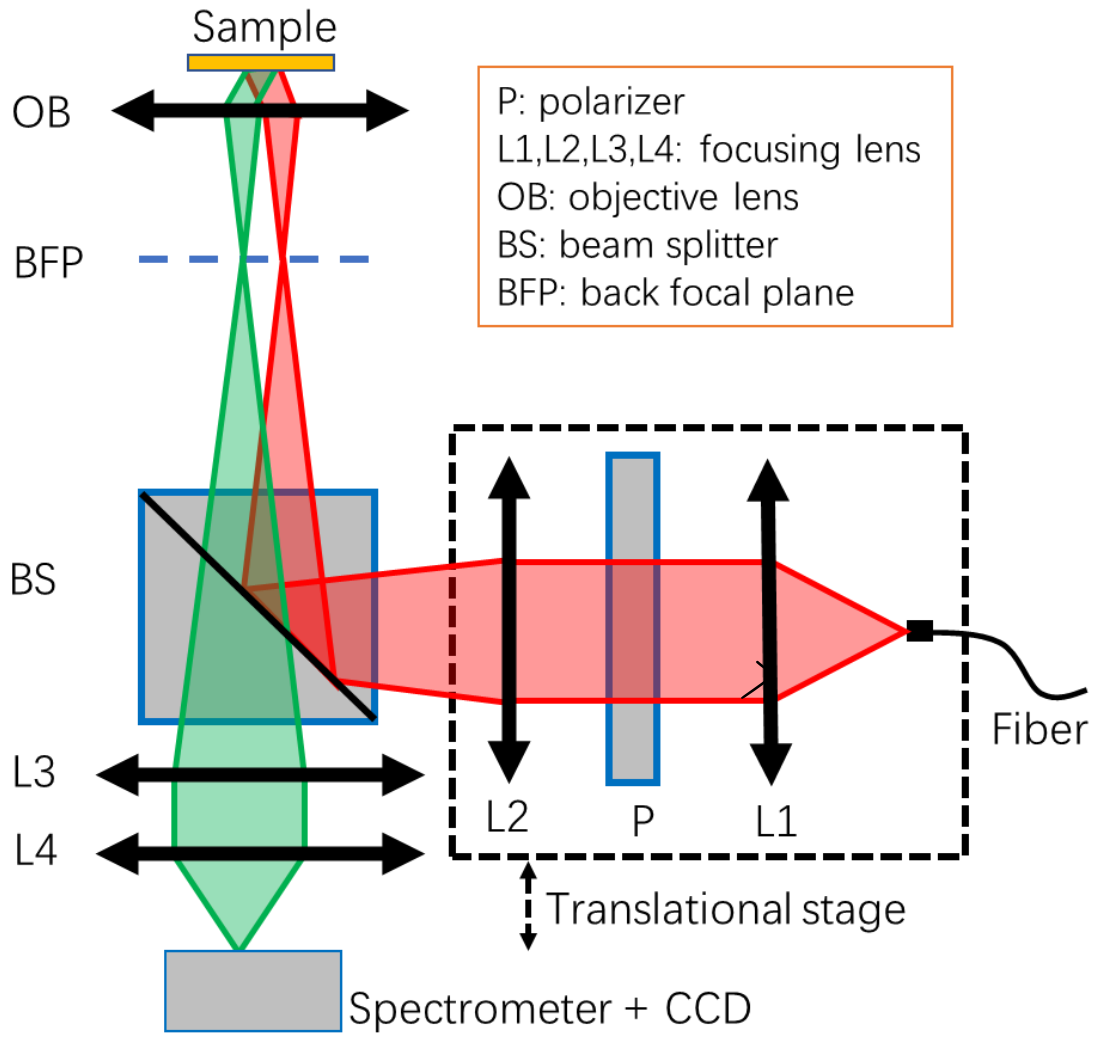


Fig. S8. The schematic of the Fourier optical microscope.

Reference

53. Z.L. Cao, S.L. Wong, S.Y. Wu, H.P. Ho, and H.C. Ong, High performing phase-based surface plasmon resonance sensing from metallic nanohole arrays, Appl. Phys. Lett. 104, 171116 (2014).